

## Aquaplanet Models on Eccentric Orbits – Effects of Rotation Rate on Observables

ARTHUR D. ADAMS,<sup>1</sup> WILLIAM R. BOOS,<sup>2</sup> AND ERIC T. WOLF<sup>3</sup>

<sup>1</sup>*Department of Astronomy, Yale University, New Haven, CT 06520*

<sup>2</sup>*Department of Earth and Planetary Science, University of California, Berkeley, CA 94720*

<sup>3</sup>*Laboratory for Atmospheric and Space Physics, Department of Atmospheric and Oceanic Sciences, University of Colorado, Boulder, CO 80309*

Submitted to AJ

### ABSTRACT

Planetary rotation rate and orbital eccentricity strongly influence planetary climate, but rotation rate is difficult to constrain from observations. This is especially true for slowly rotating planets on highly eccentric orbits, because variations in observed radiative emission caused by rotation and planet-star distance changes can have similar time scales. Here we examine how observed emission might be used to infer rotation rates in such circumstances. We employ an Earth climate model with no land and a slab ocean, and consider two eccentricities ( $e = 0.3$  and  $0.6$ ) and two rotation rates: an Earth-like period of 24 hours and a pseudo-synchronous period that generalizes spin synchronization for eccentric orbits. We adopt bandpasses of the Mid-Infrared Instrument for the James Webb Space Telescope as a template for future photometry. At  $e = 0.3$  the rotation rates can be distinguished if the planet transits near periastron, because pseudo-synchronous rotation produces a strong day-night contrast and thus an emission minimum on the observed periastron night side. However, light curves for fast and slow rotators behave similarly if the planet is eclipsed near periastron; light curves are also similar for either viewing geometry at  $e = 0.6$ . Rotation rates can nevertheless be distinguished using ratios of emission in different bands, one in the water vapor window with another in a region of strong water absorption. These ratios vary over an orbit by  $\lesssim 0.1$  dex for Earth-like rotation, but by  $0.3\text{--}0.5$  dex for pseudo-synchronous rotation because of large day-night contrast in upper-tropospheric water. For planets with condensable atmospheric constituents in highly eccentric orbits, rotation regimes might thus be distinguished with infrared emission observations for a range of viewing geometries.

### 1. INTRODUCTION

The geometry of a planet’s orbit and the rate of its rotation are both key to understanding spatial and temporal variations in the heating of its atmosphere by its host star. On Earth, the solar heating at a given position and time is dominated by the 24-hour day-night cycle from rotation, as well as the annual cycle in the orientation of the axial tilt with respect to the Sun-Earth line. These diurnal and annual cycles, with their significantly different time scales, operate largely independently of each other in the case of Earth. Additionally, Earth’s nearly circular orbit means that variations due to Earth-Sun

distance are small; Earth’s seasons are driven primarily by obliquity rather than eccentricity. Differences in orbital eccentricity, planetary rotation rate, and axial tilt can all have large consequences for atmospheric heating rates and planetary climate.

In order to extend our understanding of how planetary rotation and orbit drive periodicities in temperatures on other planets, we need to obtain observational constraints on actual rotation rates and orbits. In cases where exoplanets have been detected via both the radial velocity and transit methods, one can reliably constrain both the orbital periods and eccentricities to fairly high precision. However, very few observational constraints exist for the rotation rates of exoplanets, Earth-like or otherwise. From tidal arguments we expect Hot Jupiters on short orbital periods to undergo spin-orbit

Corresponding author: Arthur D. Adams  
[arthur.adams@yale.edu](mailto:arthur.adams@yale.edu)

synchronization<sup>1</sup> on timescales shorter than the ages of the systems (Goldreich & Soter 1966; Showman & Guillot 2002). More recently, de Wit et al. (2016) and Lewis et al. (2017) used phase photometry to constrain the range of possible rotation periods for the highly eccentric giant planet HD 80606 b. No observational constraints yet exist for the rotation rate of Earth-sized exoplanets.

The rotation rate will set both the motion of the sub-stellar point on the planet’s surface and the nature of the global atmospheric circulation that, in turn, controls planetary climate. Merlis & Schneider (2010) demonstrate that for Earth-like planets on circular orbits, Earth-like rotation periods will have larger latitudinal gradients in temperature and pressure away from the equator (see also Cullum et al. 2014). In contrast, when rotation is slow ( $P_{\text{rot}} \sim P_{\text{orb}}$ ) the surface temperature should scale with the local instellation, peaking at or near the longitude of the sub-stellar point, with weaker equator-to-pole temperature differences. At the surface, the effect of the rotation rate on the temperature should also depend on the depth of the ocean mixed layer. Bolmont et al. (2016a) explored a range of eccentricities for aquaplanet models and demonstrate that increasing the thermal inertia of the oceans damps changes in the climate more efficiently. Accordingly, faster rotation in their models reduces the sensitivity of the climate to the thermal inertia of the oceans.

We expect that, when planets on highly non-circular orbits are considered, many of the general predictions based on the broad regimes of rotation rate for circular orbits will be extensible. In the limit of slow rotation, the pseudo-synchronous rotation rate (Hut 1981) effectively “approximates” spin-orbit synchronization around the time of periastron, when stellar forcing is maximal. While the physicality of this predicted rate relies on certain assumptions and is still debated (see e.g. Makarov & Efroimsky 2013), we adopt it as an example of a rate which for most eccentricities will be much slower than an Earth-like rotation. In the fast-rotation limit, we expect that strong east-west winds induced by planetary rotation will homogenize temperatures in longitude on time scales shorter than the rate of change in instellation due to the eccentric orbit.

With current observational limitations in mind, here we seek to understand the time variation of surface and atmospheric temperatures on Earth-like planets with contrasting rotation rates and orbital shapes. Our goal is to determine whether the effects of rotation and orbit on incident radiation could induce a response which

would lead to observable differences, thereby indirectly providing a method for estimating the rotation rate when only eccentricity is constrained a priori. In the scenarios explored here we assume zero obliquity; the primary driver of seasonal variations will be eccentricity rather than axial tilt. To do so we adapt a class of 3-D models, often referred to as general circulation models (GCMs), which has been developed with Earth’s atmosphere in mind. These GCMs allow for analysis of the effects of various properties of the planetary system on the evolution of the climate (e.g. O’Gorman & Schneider 2008; Wolf & Toon 2013, 2014, 2015). Such models have also been developed for other terrestrial planets in the Solar System, particularly Venus and Mars (e.g. Rossow 1983; Barnes et al. 1993, 1996; Haberle et al. 1993; Barnes & Haberle 1996; Forget et al. 1999; Lebonnois et al. 2010; Zalucha et al. 2010; Forget et al. 2013), and have been used to explore large-scale atmospheric circulation under differences in atmospheric composition, rotation rate, and surface gravity.

Beyond the Solar System, GCMs now have a considerable history of use for possible planetary scenarios in other stellar systems. Significant modifications have been undertaken by numerous groups to accommodate unfamiliar orbital and surface conditions. Joshi et al. (1997) present an early example of a GCM applied to a hypothetical extrasolar planet, exploring the consequences of putting an Earth-like planet on a short-period, spin-synchronous orbit around a late-type star. Following this, Merlis & Schneider (2010) used a GCM to model an *aquaplanet*, an Earth-like planet with its entire surface covered by water. They examine how atmospheric dynamics change for tidally-locked planets orbiting M dwarfs, in comparison to dynamics obtained for an Earth-like, 24-hour rotation period. Such works adopt the complex representations of physics operating below the GCM grid scale (e.g. precipitating atmospheric convection and radiative transfer) that were developed for Earth to predict the behavior of exoplanet atmospheres.

In both Joshi et al. (1997) and Merlis & Schneider (2010), the authors assume a stable ocean cover for their initial conditions. The validity of this assumption is studied explicitly through the definition and continual refinement of the *Habitable Zone* (HZ), which is the range of star-planet separations for which a planet with an Earth-like radius, mass, and atmospheric composition and pressure can plausibly support liquid water oceans on its surface. The foundational works for our current HZ definition rely primarily on a 1-D radiative-convective climate model (Kasting et al. 1993; Kopparapu et al. 2013). These idealized 1-D models make some assumptions most relevant for Earth, but have

<sup>1</sup> This term is often used interchangeably with tidal locking. They are equivalent for circular orbits.

been extended to examine the effects of variations in planet obliquity (Dressing et al. 2010; Linsenmeier et al. 2015; Wang et al. 2016), planet mass (Kopparapu et al. 2014), orbital eccentricity (Kane & Gelino 2012; Linsenmeier et al. 2015; Bolmont et al. 2016a; Shields et al. 2016), host stellar spectral type and evolution (Shields et al. 2013, 2014; Wolf & Toon 2015), and the effects of clouds and their feedback (Yang et al. 2013). Those previous studies provide a wide range of theoretical predictions for the conditions governing the possible existence and persistence of liquid water oceans on terrestrial-size planets. While our purpose is not to make a critique or refinement of the currently defined HZ, we introduce it here because we will start with a range of orbital configurations currently thought to support ocean-covered planets. The two primary parameters we will vary are orbital eccentricity and rotation period, both of which have undergone substantial study in recent literature.

While GCMs can be used to explore a range of interesting and hypothetical atmospheric dynamics that might occur on exoplanets, we would like to go beyond this to make testable predictions. Here we focus on predictions that might be verified through broadband photometry, which generally offers a greater photon count over spectroscopy and therefore is invaluable for studying faint and small, warm-to-cool exoplanets. Many giant planets on extremely short orbits have been observed indirectly via transits and secondary eclipses, and in some cases have been examined over significant fractions of their orbits. While transit detections have substantially increased the population of known extrasolar planets, secondary eclipse measurements provide a complementary set of data that helps constrain major properties of planets' emissions. From the depth of a planet's eclipse we can infer the temperature of its illuminated hemisphere, which gives clues to the atmospheric conditions. A key instrument for observing secondary eclipses has been the Spitzer Space Telescope's Infrared Array Camera (IRAC) (Werner et al. 2004), which has 4 photometric bands spanning 3.6–8.0  $\mu\text{m}$ . In some opportune cases Spitzer has been able to observe planets over full orbits in some combination of these bands, providing a temporal connection between night-side observations of a planet in transit and day-side observations of it in eclipse.

Taking inspiration from these current observational techniques, here we generate predictions of eclipse depths and phase photometry from an exoplanet GCM. In particular, we examine how rotation rate and orbital eccentricity control, via the global atmospheric circulation, the radiative properties of a planet's surface and atmosphere. We explore whether a detailed treatment

of the complex atmospheric circulation and radiative transfer allow us to infer the rough scale of rotation rate from a limited set of observable features.

We begin by describing our assumptions for both orbital eccentricity and planetary rotation rate, along with relevant background, in §2. In §3 we describe the GCM we employ, and how we use it to simulate observable quantities. We present our results in §4, focusing on both the internal properties of the planetary atmospheres and the consequent observables.

## 2. ASSUMPTIONS OF ROTATION AND ORBIT

### 2.1. Orbital Eccentricity

Numerous HZ planets are known to have nonzero orbital eccentricity (Adams & Kane 2016). The role of the Lidov-Kozai mechanism (Kozai 1962; Lidov 1962) for increasing the orbital eccentricity of terrestrial planets is explored in Spiegel et al. (2010), and subsequently in works such as Georgakarakos et al. (2016), Way & Georgakarakos (2016), and Deitrick et al. (2018). The process allows for the existence of highly eccentric Earth-sized planets with neighboring giant planets; orbital resonances between the planets and their mutual proximities are the two critical components to the mechanism's efficiency (Murray & Dermott 1999).

Williams & Pollard (2002) argue that the instellation time-averaged over an orbit is the primary determinant of whether liquid water can be sustained on a terrestrial planet's surface. For eccentric orbits the mean-flux approximation (MFA) fixes the time-averaged instellation over an orbit to that of a reference planet on a circular orbit. When comparing the flux  $F$  with that of Earth, as a function of the stellar luminosity  $L_*$ , semi-major axis  $a$ , and eccentricity  $e$ ,

$$\left\langle \frac{F}{F_\oplus} \right\rangle = \frac{L_*/L_\odot}{(a/a_\oplus)^2 \sqrt{1-e^2}} \quad (1)$$

where the reference values for Earth are taken to be  $F_\oplus = 1360 \text{ W m}^{-2}$ ,  $L_\odot = 3.83 \times 10^{26} \text{ W}$ , and  $a_\oplus = 1 \text{ AU}$ . Triangle brackets denote a time average over an orbit. Barnes et al. (2008) use the conclusion of Williams & Pollard (2002) to define an *Eccentric HZ* (EHZ) by scaling the semimajor axis  $a$  with eccentricity according to the MFA (Equation 1). All models presented here have their semimajor orbital axes (and, by extension, orbital periods) set according to this approximation.

### 2.2. Rotation Rate

For planets on eccentric orbits, Hut (1981) presents a limiting rotation rate based on a tidal evolution argument, analogous to the synchronous limit for circular orbits. The *pseudo-synchronous* rotation (PSR) period is

**Table 1.** Orbital properties for pseudo-synchronously rotating planets with Earth-like mean instellation. The bold entries correspond to the scenarios explicitly modeled in this work.

$e$	$a$	$P_{\text{orb}}$	Peak Instellation	
			(days)	( $P_{\text{orb}}$ )
<b>0.3</b>	<b>1.024</b>	<b>378.35</b>	<b>242.98</b>	<b>0.642</b>
0.4	1.045	389.88	190.65	0.489
0.5	1.075	406.81	145.01	0.356
<b>0.6</b>	<b>1.118</b>	<b>431.74</b>	<b>105.89</b>	<b>0.245</b>
0.7	1.183	470.11	72.30	0.154
0.8	1.291	535.70	43.45	0.081
0.9	1.515	680.78	18.96	0.028

calculated from this pseudo-synchronous rate, and may be written in units of the orbital period as

$$\frac{P_{\text{PSR}}}{P_{\text{orb}}} = \frac{\left(1 + 3e^2 + \frac{3}{8}e^4\right) \left(1 - e^2\right)^{3/2}}{1 + \frac{15}{2}e^2 + \frac{45}{8}e^4 + \frac{5}{16}e^6}. \quad (2)$$

In the circular orbit limit ( $e \rightarrow 0$ ), the spin frequency matches the orbital frequency, with a ratio  $P_{\text{PSR}}/P_{\text{orb}} \rightarrow 1$ . As  $e \rightarrow 1$ , this ratio approaches zero. For modest eccentricities the ratio is of order unity; here we consider such cases of rotation rate as characteristically “slow” rotators. For higher eccentricities the ratio decreases precipitously, but only reaches periods as short as an Earth day under the MFA for  $e > 0.99$  (Figure 1). Therefore, for all eccentricities modeled in this work, we use an Earth-like rotation period as characteristically “fast” rotation for comparison<sup>2</sup>.

At high eccentricities, the sub-stellar point on the planet’s surface exhibits a peculiar “retrograde motion” around periastron due to the relation between the planet’s rotation rate and the variable rate of change in true anomaly. This rate of change  $\dot{\nu}$  at periastron relative to the mean rate  $\bar{\omega}_{\text{orb}} \equiv 2\pi/P_{\text{orb}}$  is

$$\frac{\dot{\nu}_{\text{peri}}}{\bar{\omega}_{\text{orb}}} = \sqrt{\frac{1+e}{(1-e)^3}}. \quad (3)$$

This value is 5 for  $e = 0.6$ , compared with roughly 4 for  $\omega_{\text{rot}}/\bar{\omega}_{\text{orb}}$ . This transient increase in the rate of change in true anomaly, which exceeds the rotation rate, causes the sub-stellar point to temporarily reverse direction from its otherwise westward motion. Figure 2 shows this effect on the sub-stellar longitude as a function of eccentricity.

<sup>2</sup> The terms “PSR” and “slow” rotation will be used interchangeably throughout this work, as well as “Earth-like” (or  $\oplus$ ) and “fast”.

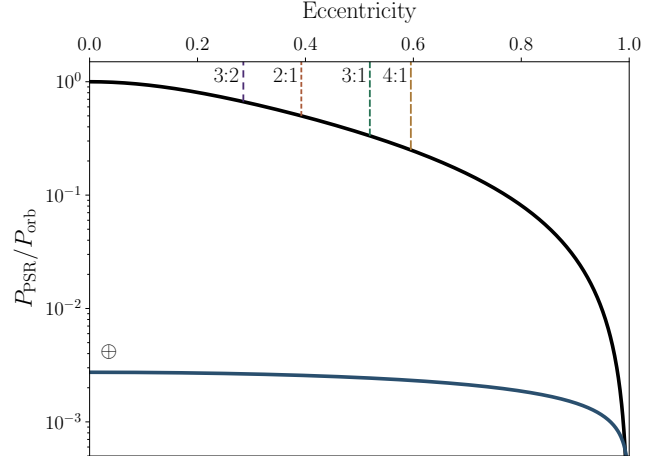


**Figure 1.** The theoretical pseudo-synchronous rotation period matches the synchronous period (orbital period) for a circular orbit, and remains on the order of the orbital period until very high eccentricity, where the ratio (shown in black) drops precipitously as  $e \rightarrow 1$ . Here we assume the orbital period scales with the Mean-Flux Approximation (Equation 1), which preserves the orbit-integrated instellation as eccentricity is changed. The ratio corresponding to a rotation period of 1 Earth day is shown as the curve in blue, labelled as  $\oplus$ . The values of eccentricity corresponding to spin-orbit resonances of 3:2 ( $e = 0.285$ ), 2:1 ( $e = 0.392$ ), 3:1 ( $e = 0.519$ ), and 4:1 ( $e = 0.595$ ) are marked.

### 3. MODEL DETAILS

The National Center for Atmospheric Research (NCAR) Community Atmospheric Model (CAM) is a global climate model designed to simulate Earth’s atmosphere (Neale et al. 2010), and is the atmospheric component of the fully coupled Community Earth System Model (CESM). This atmospheric GCM uses a Finite Volume Dynamical Core, described in Chapter 3 of Neale et al. (2010). Its horizontal discretization uses a semi-Lagrangian flux transport scheme (Lin & Rood 1996, 1997), while the vertical discretization is termed *quasi-Lagrangian* due to a coordinate remapping. The atmospheric dynamics are computed from the primitive equations of fluid motion on a sphere.

Here we use an adaptation of the ExoCAM<sup>3</sup> extension of CAM 4. Short for Exoplanet CAM, ExoCAM is designed for studies of both Earth paleoclimates and exoplanets with particular attention to expanding the valid ranges of stellar forcing, atmospheric partial pressure of greenhouse constituents ( $\text{H}_2\text{O}$ ,  $\text{CO}_2$  and  $\text{CH}_4$ ) (Wolf & Toon 2013, 2014), and planetary rotation rate. These modifications improve the deep convection scheme to

<sup>3</sup> <https://github.com/storyofthewolf/ExoCAM>

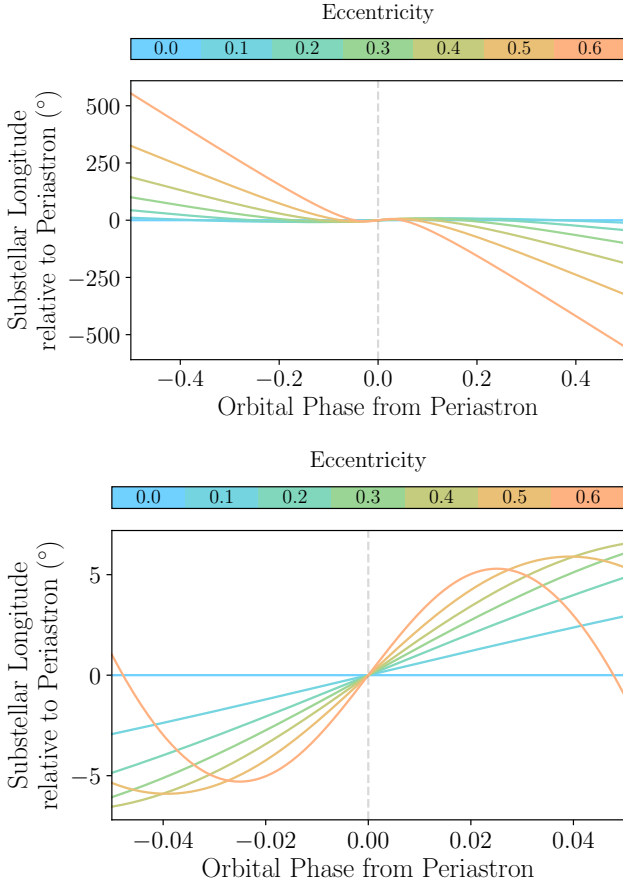


**Figure 2.** Eccentric orbits have periodically varying rates of change in the planet’s orbital anomaly, with a maximum rate at periastron. For slow enough rotation (e.g. pseudo-synchronization), there exists a region of time around periastron where the instantaneous change in anomaly exceeds the rotation rate, causing the sub-stellar point on the planet’s surface to move eastward rather than westward. This region is broad and the effect minor for nearly circular orbits, but narrow and increasingly intense at higher eccentricity. The plots show the movement of the sub-stellar longitude relative to its periastron position, both for one full orbit (top) as well as for a small region of orbital phase space around periastron (bottom), to show the effects at high eccentricity.

allow for warm and moist greenhouse conditions, with mean surface temperatures  $\lesssim 365$  K and water vapor partial pressures  $\lesssim 200$  hPa.

Our version of the model is closely aligned with the configuration described in Kopparapu et al. (2017). The horizontal resolution is  $4^\circ \times 5^\circ$ , with 40 vertical levels ranging from a global mean surface pressure around 1000 hPa to a minimum pressure of 1 hPa. We employ a commonly used aquaplanet configuration for simplicity: we fix the planetary radius and surface gravity to Earth values, and have flat topography with a uniform-depth slab

**Table 2.** Wavelength Ranges of Model IR Spectral Bands

Band	$\lambda_{\text{start}}$	$\lambda_{\text{mid}}$	$\lambda_{\text{end}}$	Brightness Temp.
	( $\mu\text{m}$ )	(K)		
1	2.50	2.76	3.08	942–1159
2	3.08	3.42	3.84	753–942
3	3.84	4.02	4.20	690–753
4	4.20	4.37	4.55	638–690
5	4.55	4.67	4.81	603–638
6	4.81	5.15	5.56	522–603
7	5.56	6.10	6.76	429–522
8	6.76	6.97	7.19	403–429
9	7.19	7.78	8.47	342–403
10	8.47	8.77	9.09	319–342
11	9.09	9.62	10.20	284–319
12	10.20	11.11	12.20	238–284
13	12.20	13.16	14.29	203–238
14	14.29	15.04	15.87	183–203
15	15.87	17.70	20.00	145–183
16	20.00	21.62	23.53	123–145
17	23.53	25.81	28.57	101–123
18	28.57	36.36	50.00	58–101
19 <sup>a</sup>	50.00	525	1000	3–58

<sup>a</sup> Band 19 of the longwave output is not considered in our analysis, but included here for completeness.

ocean (Bitz et al. 2012). Most of our simulations use an ocean depth of 50 meters; we also run the  $e = 0.3$  cases with ocean depths of 10 meters to study how our results change with ocean depth. Ocean heat transport is neglected, but the model does account for sea ice formation, the implementation of which is the CICE model from Hunke E.C. (2008). The water ocean albedo in both the visible and near-IR is tuned to 0.06 for direct and 0.07 for diffuse reflection, matching the values established in Shields et al. (2013). The radiative transfer code uses the HITRAN 2012 spectral database (Kopparapu et al. 2017) with the solar spectrum. The spectral binning is divided roughly into the “shortwave”, encompassing the solar spectrum out to  $3.84\ \mu\text{m}$ , and “longwave”, which we list in Table 2 in order to discuss the planet’s thermal emission.

### 3.1. Orbital Configuration

We modify the orbital calculations used in the standard ExoCAM code to ensure greater accuracy at high orbital eccentricities. For high orbital eccentricities, calculating the orbital position is crucial for correctly modeling the sub-stellar position and time-dependent instellation. By default, CESM calculates the true longitude

(also known as the *true anomaly* for exoplanets) of the Earth using an approximation given by a third-order polynomial,

$$\begin{aligned}\lambda = M + \left(2e - \frac{e^3}{4}\right) \sin(M + \varpi) \\ + \frac{5e^2}{4} \sin[2(M + \varpi)] \\ + \frac{13e^3}{12} \sin[3(M + \varpi)],\end{aligned}\quad (4)$$

where  $M$  is the mean anomaly,  $e$  is the orbital eccentricity, and  $\varpi$  is the longitude of periastron. This approximation is valid to  $\lesssim 0.3\%$  for eccentricities up to 0.1. However, the approximation rapidly diverges from the exact result, with the error reaching  $\approx 12\%$  at  $e = 0.5$ , and  $\approx 83\%$  at  $e = 0.95$ . We replace the approximation with a simple numerical method that iteratively solves Kepler's equation,

$$M = E - e \sin E,\quad (5)$$

where  $E$  is the eccentric anomaly.

### 3.2. Observable Properties

We now describe how we simulate the radiation that would be observed by a telescope at a location distant from the planet and star of interest. Exoplanetary systems can in general have any possible orientation with respect to the observer. For our analyses we restrict ourselves to 2 lines of sight for full-phase modeling, both edge-on with respect to the orbital plane: one along the periastron-star line and another along the apastron-star line. Such an assumption amounts to varying the longitude of periastron while keeping other orientation parameters fixed. In the first case (corresponding to an inclination  $i = 90^\circ$ , longitude of periastron  $\varpi = 90^\circ$ ), one would observe the night side of the planet during periastron, when the planet would transit its host star; then, one would be able to see the day side during apastron, when the planet passes through its secondary eclipse. In the second case ( $i = 90^\circ$ ,  $\varpi = 270^\circ$ ), the day side at periastron is visible during eclipse (or more precisely, just before and after eclipse), and the night side at apastron during transit. In addition to these two cases, we also generate theoretical eclipse depths for the full possible range of longitudes of periastron, in order to show the variation in day-side emission with viewing geometry.

To generate theoretical light curves, we take the outgoing radiation maps in each model band and calculate the expected observable flux for the two previously described viewing geometries. We use a blackbody spectrum for the model host star to then express our expected brightnesses in units of the thermal stellar flux.

To compare with a realistic set of observations in the infrared, we adopt the wide filter profiles (Institute 2017) for the Mid-Infrared Imager (MIRI) on the James Webb Space Telescope (JWST) (Rieke et al. 2015; Wright et al. 2015; Glasse et al. 2015). These filters span a range of approximately 5–30  $\mu\text{m}$ . Convolving these filter profiles with the model bands, we generate emission maps for each JWST MIRI band. Given an emission map  $M_\lambda(\phi, \theta, t)$  at a specific wavelength, we solve for the corresponding planet-star flux contrast via

$$\bar{F}(t) = \left(\frac{R_p}{R_*}\right)^2 \frac{\iiint \lambda w M_\lambda V d\lambda d\theta d\phi}{\iiint \lambda w M_\lambda V d\lambda d\theta d\phi} \quad (6)$$

where  $w = w(\lambda)$  is the weighted response of the instrumental bandpass at  $\lambda$ , and  $V = V(\phi, \theta, t)$  is the component of the normal vectors of the cells along the line of sight. For a sub-observer point given by longitude  $\phi_{\text{obs}} = \phi_{\text{obs}}(t_0) - \omega_{\text{rot}} t$  with initial time  $t_0$  and rotation rate  $\omega_{\text{rot}}$ , and latitude  $\theta_{\text{obs}} = 0$ ,

$$V = \begin{cases} \cos(\phi - \phi_{\text{obs}}) \cos \theta, & \cos(\phi - \phi_{\text{obs}}) \leq \pi/2 \\ 0, & \cos(\phi - \phi_{\text{obs}}) > \pi/2 \end{cases} \quad (7)$$

Once we have a full orbit of predicted photometry, we select the contrasts during eclipse as our predicted eclipse depths.

Each model is run for 25 orbital periods; this value was chosen as the longest time needed (across all of our integrations) for the range of global mean, time mean surface temperatures for each of a span of 10 orbits to be within 1% of the global mean, time mean temperature averaged over the same 10-year span. The model photometry we present uses statistics calculated for the final 10 orbits of each simulation.

## 4. RESULTS

### 4.1. Internal Results

In this section we describe the simulated climate of our four hypothetical planets, then illustrate a key difficulty in interpreting observations of such planets: temperatures in the upper troposphere near the emission level vary because of both day-night contrast and orbital periodicity, with the amplitude and phase of these variations being highly sensitive to orbital eccentricity.

#### 4.1.1. Surface Conditions

Rotation rate strongly influences horizontal temperature gradients, as expected, with fast rotation confining warm air near the equator and producing strong eastward winds that homogenize energy content in longitude. This is clearly seen in the distributions of surface

temperature and surface albedo, with the latter indicating the regions covered by sea ice on these aquaplanets (Figure 3 and Table 3). Temperature and albedo contrasts are primarily latitudinal for Earth-like rotation, and are accompanied by a Hadley circulation with a rising branch centered on the equator (not shown). For slow, pseudo-synchronous rotation, longitudinal contrasts are just as strong as latitudinal ones, with warm, ice-free ocean centered on the sub-stellar point at periastron and ice-covered regions extending over the night side and polar regions. At apastron, the effects of ocean thermal inertia and deviations from strict synchronous rotation combine to shift the warm, ice-free region away from the sub-stellar point. For  $e = 0.3$  and PSR, the ice-free region straddles the day-night line at apastron; for  $e = 0.6$  and PSR the ice-free region is actually on the night side of the planet at apastron while the day side is ice-covered and has a secondary temperature maximum of about  $-20^\circ\text{ C}$  at the sub-stellar point.

The horizontal range in surface temperature at both extremes of the orbit is larger for the Earth-like case than for PSR, implying that rotational confinement by the atmospheric circulation is more effective at generating horizontal temperature gradients than the day-night contrast in radiative heating. In fact, both the range and global mean of surface temperatures for the  $e = 0.3$ , PSR case are remarkably similar between apastron and periastron. The differences in apastron-to-periastron global mean temperature for the Earth-like cases, in contrast, exceed  $20^\circ\text{ C}$  for both eccentricities.

#### 4.1.2. Atmospheric Conditions

Temperature contrasts between the day and night side of the slow (pseudo-synchronous) rotator are even more muted in the atmosphere above the lowermost troposphere (Figure 4, right column). This is expected because the Rossby deformation radius is larger than the planetary circumference at these rotation rates, allowing atmospheric circulations to rapidly homogenize temperatures throughout most of the troposphere, as in previous studies of strict synchronous rotation (Joshi et al. 1997). But in contrast with those previous studies, the shallow, near-surface temperature inversion that forms on the ice-covered side of the planet is actually on the day side of the planet at apastron (see bottom right panel of Figure 4), due to the combined effects of ocean thermal inertia and deviations from strict synchronous rotation, as discussed above.

To illustrate how these effects might complicate interpretation of observations, we plot time series over an orbit of the day- and night-side temperatures averaged over an atmospheric layer near the emission level, which

we estimate to be  $\sim 300$  hPa (Figure 5). In an optically thick atmosphere, radiative emission might come from this upper-tropospheric layer, making its temperature more relevant to observations than surface conditions. The behavior of the fast rotator is easy to understand, with day- and night-side temperatures being nearly equal, and peak temperatures reached shortly after periastron for both eccentricities. For the slow rotator, the day-night contrast in upper-level temperature is also very small, and the orbital variations in emission from this level are due almost entirely to changes in planet-star distance. It would thus be difficult to distinguish a fast rotator from a slow rotator given only emission from this upper-tropospheric level. In contrast, surface temperature exhibits a large contrast between day side and night side on the slow rotators. Night-side surface temperature has the same range as 300 hPa temperature but with the opposite phase for  $e = 0.3$ ; for  $e = 0.6$ , night-side surface temperatures for the slow rotator show several peaks over an orbit, corresponding to the roughly four rotations that occur over an orbit at this eccentricity (Fig. 1). Thus, inferences about rotation rate would be most easily made from the day-night contrast in surface temperature, but it is possible that emission will come from a much higher altitude.

The troposphere of the slow (pseudo-synchronous) rotator exhibits a much wider longitudinal contrast in water content than in temperature (Figure 4, left column). As we move from the surface to the upper troposphere, the slow rotator retains a much moister troposphere on the day side at periastron, even though temperatures are nearly equal above the lower-tropospheric inversion layer. This is also true at apastron for  $e = 0.3$ , but for  $e = 0.6$  at apastron the humidity is higher over the open ocean on the night side and lower on the day side over the ice-covered surface. Considering the slowly rotating case further, we notice that the strong wet-dry difference extends to  $\sim 100$  hPa at periastron for  $e = 0.3$ , compared with  $\sim 300$  hPa at apastron. This reflects the large warming and deepening of the troposphere over the sub-stellar point when the radiative forcing is strongest at periastron. The day-night humidity contrast seen on the slow rotator is even more pronounced at higher eccentricity, reaching to  $\sim 30$  hPa. The upper troposphere at apastron is warmer and more humid at the sub-stellar point than at the anti-stellar point, even though the converse is true at the surface and in the lower troposphere, showing the complexity introduced to day-night contrasts by pseudo-synchronous rotation.

Given these strong day-night contrasts in humidity, it is not surprising that the slow rotators at both eccentricities show extremely large cloud water paths, approach-

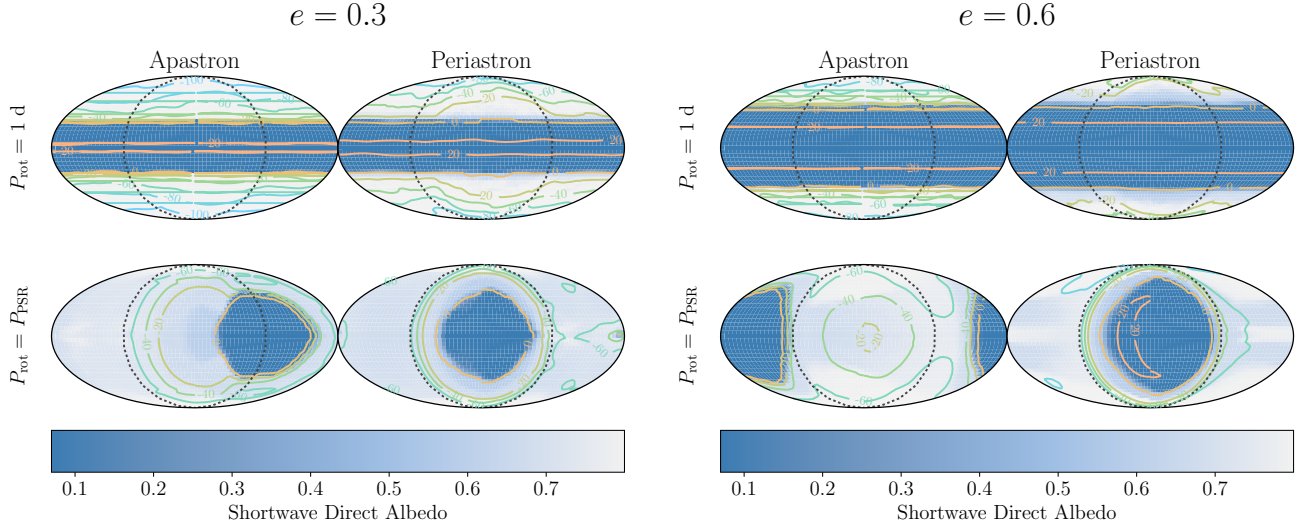


**Figure 3.** Global maps of the diffuse shortwave albedo at the surface at the extreme points of each orbit, for each of two rotation periods (Earth-like in the upper row, and the pseudo-synchronous period defined in Equation 2 in the lower) and orbital eccentricities of 0.3 and 0.6. The dark dotted lines delineate the star-facing hemisphere, which is centered in each plot. Colored contours denote surface temperature in Celsius. The nominal albedo for liquid water is taken to be 0.06–0.07 (see §3 for details), and the limiting albedo for thick ice cover is 0.8.

**Table 3.** Global Ranges and Means of Surface Temperature (K)

e	Time	$\oplus$			PSR		
		Range	Mean	Ocean Mean <sup>a</sup>	Range	Mean	Ocean Mean <sup>a</sup>
0.3	Apo	155–295	220	288	198–286	228	280
	Peri	170–295	241	289	195–285	228	278
0.6	Apo	183–305	248	292	200–287	228	280
	Peri	214–305	271	293	191–298	232	285

<sup>a</sup>The ocean mean is defined as the global mean of all regions with  $T > 273.15$  K.

ing  $1 \text{ kg m}^{-2}$ , centered on the sub-stellar point at periastron (Figure 6), largely mimicking the features seen in both surface temperature and albedo. The negative cloud forcing in the shortwave is presumably responsible for limiting sub-stellar surface temperatures at periastron, causing the peak ocean temperatures to exist in a partial ring around the sub-stellar point (Figure 3).

Taken together, all of these quantities show that slowly rotating planets on orbits of modest to high eccentricity can become mostly ice covered, except for a longitudinally confined warm, cloudy, and ice-free region that persists at low latitudes through the orbit. This is consistent with previous simulations of synchronously rotating aquaplanets on circular orbits (e.g. Joshi et al. 1997; Merlis & Schneider 2010) and on eccentric orbits (Bolmont et al. 2016b), except that

the ice-free region does not remain on the day side at apastron for pseudo-synchronous rotation (see §4.2.2 for further discussion). The implications of this shift in the warm, ice-free region for observable emission is further complicated by the fact that atmospheric temperatures vary much more than surface temperatures over the orbit (e.g. Figure 4), responding to the orbital cycle of insolation. In contrast, for faster, Earth-like rotation, all quantities are homogenized zonally, so that outgoing radiation will be set by the orbital variations in stellar heating.

## 4.2. External Results

### 4.2.1. Outgoing Longwave Radiation

As an intermediate step between characterizing the atmospheric state and simulating what might be observed by

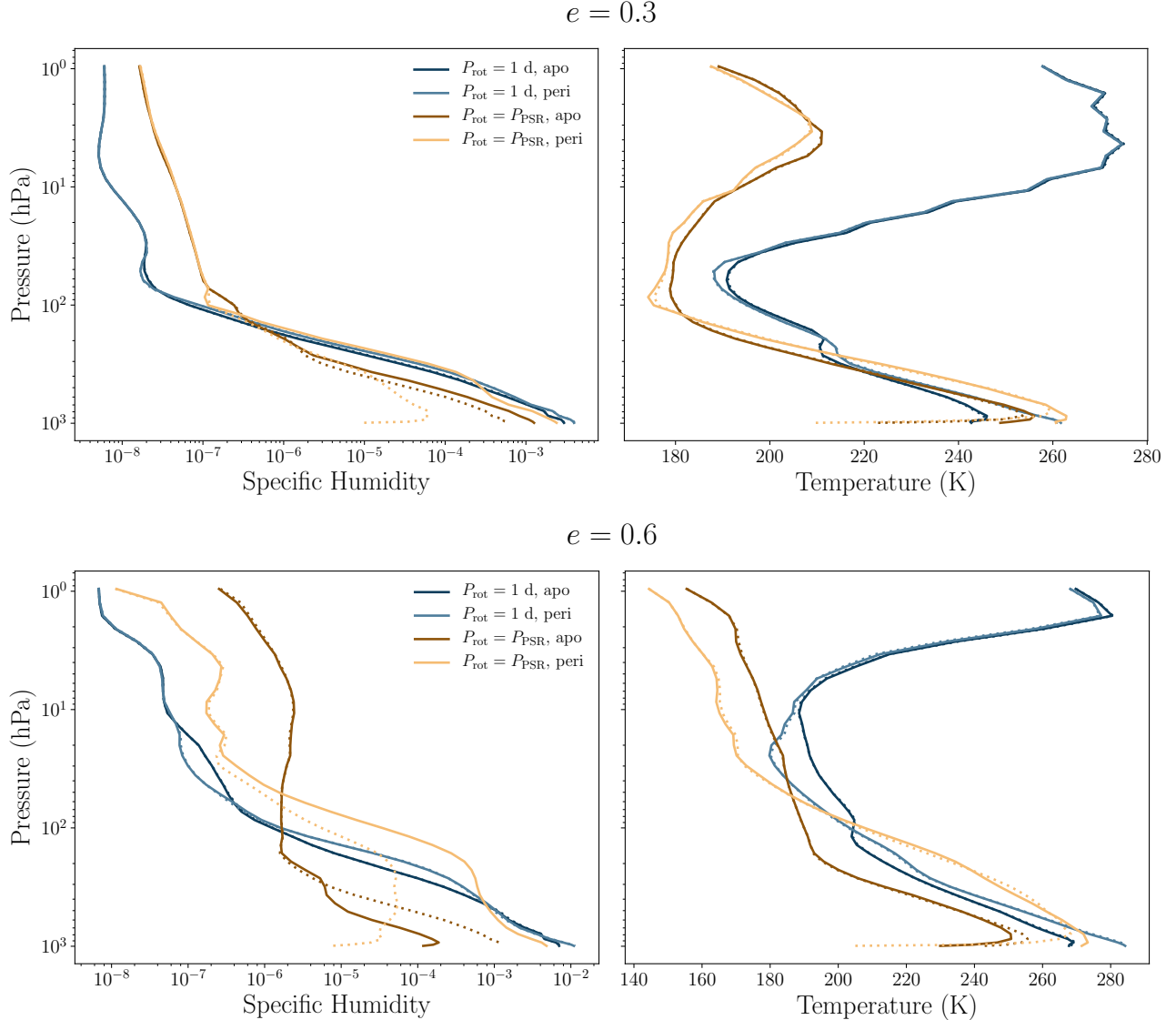


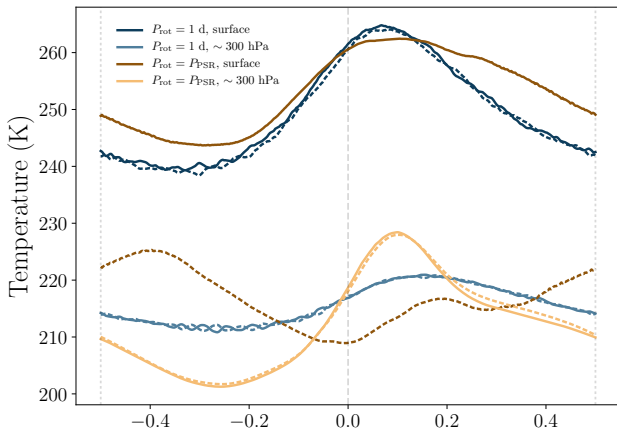
**Figure 4.** The specific humidity (fraction of atmospheric mass in  $\text{H}_2\text{O}$ ) and temperature, both averaged over the day sides (solid lines) and night sides (dotted lines). Each color represents a rotation period, with the lighter lines showing the quantities during periastron, and the darker lines those during apastron.

a telescope, we examine the horizontal distribution of planetary radiative emission in the spectral bins used by the model radiation scheme. The peak radiative flux in each spectral bin is similar (within  $\pm 50\%$ ) across rotation rates and orbital phase. The fast rotators have emission that is nearly uniform in longitude with a large equator-to-pole gradients, as expected. In contrast, for PSR cases, the night-side fluxes at most wavelengths remain much lower when compared to either the PSR day side fluxes or the fluxes in the polar regions of the fast rotators (Figure 7). In all bands, the PSR sub-stellar point is an emission minimum due to the thick cloud shield,

and the maximum emission occurs in a ring closer to the edge of the day side.

The contrast between night side emission and the emission from this ring at the edges of the day side is weaker in the  $6.97$  and  $7.78 \mu\text{m}$  bands, which both lie in the water vapor absorption band that is centered at  $6.3 \mu\text{m}$  (and which, in turn, absorbs strongly between  $5$  and  $8 \mu\text{m}$ ). In these spectral regions, the dryness of the atmosphere on the cold night side allows radiation to escape from the lower troposphere or the surface itself, while the high optical depth on the warm day side allows emission only from higher (and thus colder) levels of the upper-troposphere. The day-night contrast for

$$e = 0.3$$



$$e = 0.6$$

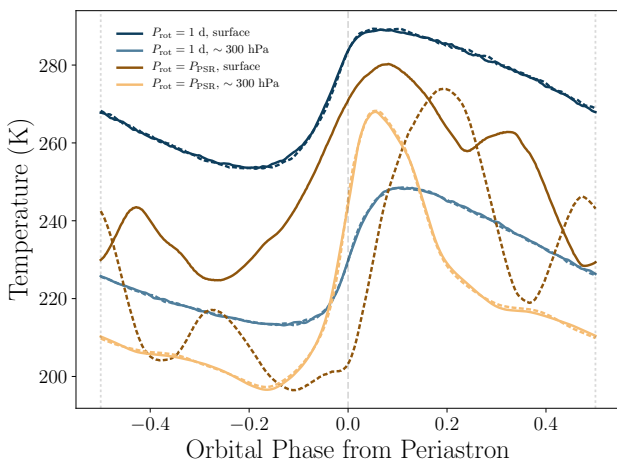


**Figure 5.** Time series of hemispherically-averaged temperatures over one orbit. Lighter colors are the temperatures at the effective emission layer (taken to be centered at  $\sim 300$  hPa, averaged over 200–400 hPa), and darker colors are surface temperatures. The solid lines are the averages over the day sides and the dotted lines the averages over the night sides. At the surface, day-night contrasts in temperature are comparable in amplitude to the variations due to the orbital periodicities in instellation. However in the upper troposphere, from where outgoing longwave emission may originate in many spectral bands, the day-night contrasts are effectively negligible.

PSR also weakens for the same reasons as we move out beyond  $20 \mu\text{m}$ , into the reddest bands occupied by the rotational absorption features of water.

These emission distributions show that the strong longitudinal temperature contrasts in our slow rotators are best observed in longwave bands away from the major water vapor absorption features. When considering ob-

servables, it must also be borne in mind that for PSR, the warm side will not always be the day side (e.g. Figure 3). Emission changes caused by planet-star distance variations over an orbit may also complicate the inferences that can be made about rotation rate from observables. This motivates construction of simulated light curves in the next section.

#### 4.2.2. Observable Light Curves

Adopting the methodology of converting model output to photometry, we generate light curves for JWST-like MIRI filter profiles for the two assumed viewing geometries described in §3.2. Figure 8 shows the model light curves at both eccentricities for a viewing geometry where the planet’s transit and periastron passage coincide ( $\varpi = 90^\circ$ ), and Figure 9 shows light curves for a geometry where eclipse and periastron passage coincide ( $\varpi = 270^\circ$ ). We discuss four primary qualities of these light curves:

1. For Earth-like rotation, the variation follows the expectation for a longitudinally symmetric system in which the flux follows the variations in planet-star distance over the orbital cycle, modified by the viewing geometry. Accordingly, the light curve variations have significantly higher amplitude at higher eccentricity (note the change in vertical scale between eccentricities in Figures 8 and 9). The light curves for fast rotators reach their peak at or shortly after apastron, when the planet is closest to the star and thus hottest, and the light curve morphology is largely independent of wavelength.
2. For pseudo-synchronous rotation, the phase variations are more complicated but are generally affected strongly by the longitudinal temperature contrasts. Where eclipse aligns with periastron and thus the observer sees the day side (corresponding to  $\varpi = 270^\circ$ , in Figure 9), the light curves have maxima at or just after periastron, giving the pseudo-synchronous light curves similar times of extrema to the Earth-like rotators for both eccentricities. Conversely, where eclipse is aligned with apastron ( $\varpi = 90^\circ$ , Figure 8) the light curves reach an absolute minimum near periastron. For  $e = 0.3$  the PSR light curves are nearly  $180^\circ$  out of phase with the light curves for Earth-like rotation. In contrast, for  $e = 0.6$  the flux quickly brightens after the periastron minimum as the rotation in this part of the orbit brings the highly irradiated hemisphere into view, resulting in the maxima of the PSR light curves occurring

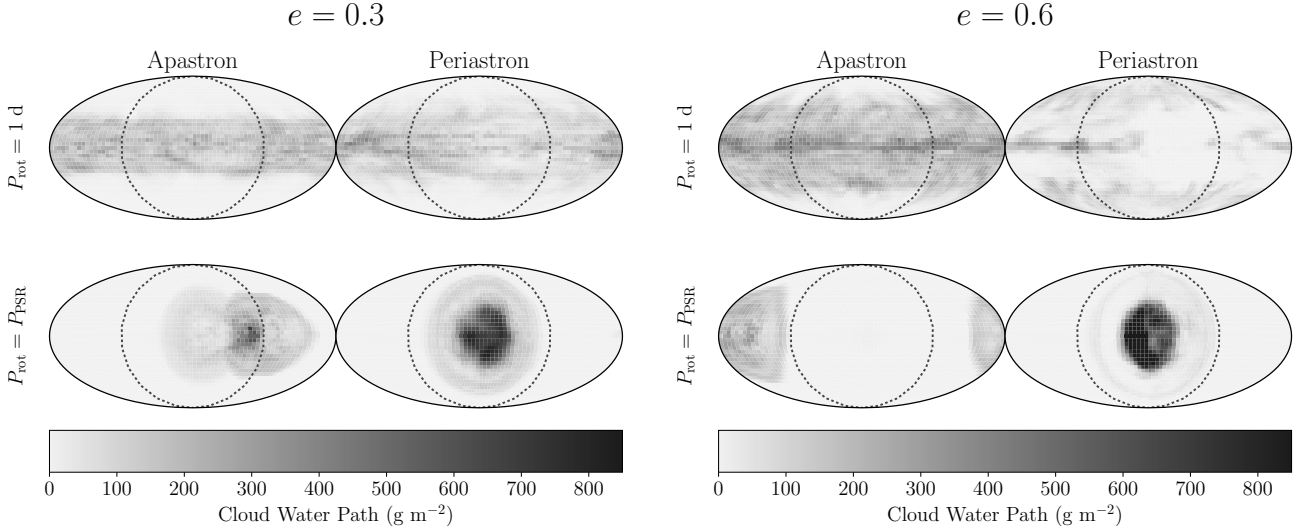


**Figure 6.** Global maps of the vertically integrated condensed cloud water at the extreme points of each orbit, for each of two rotation periods (Earth-like in the upper row, and the pseudo-synchronous period defined in Equation 2 in the lower row) and orbital eccentricities of 0.3 and 0.6. The dark dotted lines delineate the star-facing hemisphere, which is centered in each plot.

at nearly the same orbital phase as the maxima of light curves for Earth-like rotation.

3. The PSR fluxes are consistently lower than their Earth-like counterparts for  $\varpi = 270^\circ$  and for the high-eccentricity curves with  $\varpi = 90^\circ$ . This is consistent with the PSR cases having ice-covered sides substantially colder than the mean temperature of the fast rotators (Figure 3 and Table 3), as well as much higher upper-tropospheric humidities (Figure 4) on the warm sides of the planets, and therefore much higher cloud water paths (Figure 6).
4. The simple thermal expectation is that, as the bands move toward longer wavelengths, the contrast ratio will increase. We see this in both rotation rates, but additional wavelength-dependent features are present for PSR in particular that affect the shapes of the periastron-induced maxima for  $\varpi = 270^\circ$ . For example, in the  $e = 0.3$  light curves for the slow rotator, there are peaks shortly after periastron consistent with  $\text{H}_2\text{O}$  emission in the F770W band (centered at  $7.7 \mu\text{m}$ ) and at wavelengths longer than  $18 \mu\text{m}$ . The order of magnitude increase in upper-atmosphere moisture content (as seen in Figure 4) provides the slower rotators with the water vapor needed to intensify the observed flux in this band.

Beyond these major features, some additional qualities of the light curves warrant explanation. Secondary peaks occur in most of the PSR light curves and come

from the ratio of the rotation period to the orbital period. This creates a single secondary peak for  $e = 0.3$ , where the ratio is  $\approx 0.64$  (i.e. roughly 2 rotations each orbital period), and 3 secondary peaks for  $e = 0.6$ , where the rotation period is close to one-quarter the orbital period.

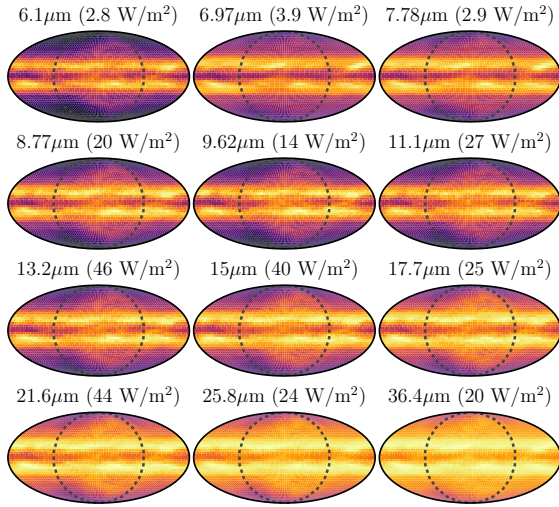
#### 4.2.3. Constructing Light Curve Ratios

With all of the above features in mind, we construct “colors” by comparing the fluxes in two bands. Here we choose two pairs of bands: the bands at  $7.7$  and  $10.0 \mu\text{m}$ , and the bands at  $12.8$  and  $18.0 \mu\text{m}$  (Figures 10–11). Each of these pairs compares one band where water has a strong absorption feature with another band in the water vapor window. For the first pair, which consist of shorter wavelengths, the longer-wavelength band is in the water vapor window while the shorter lies in the  $6.3 \mu\text{m}$  water vapor vibrational-rotational absorption band. The converse is true of the second pair of bands, which lie at longer wavelengths: the shorter-wavelength band is in the water vapor window and the longer band lies in the short-wavelength end of the pure rotational, far-infrared absorption band of water vapor. The behavior of these colors are discussed in greater detail in Appendix A.

For a transit-periastron viewing angle ( $\varpi = 90^\circ$ ) we see a consistent difference in the colors during or near periastron. The differences can be as high as 0.35 dex for both eccentricities. At  $\varpi = 270^\circ$ , the peak difference between slow and fast rotators is not well-aligned with periastron for  $e = 0.3$ , reaching a maximum notably prior to transit and having a smaller secondary maxi-

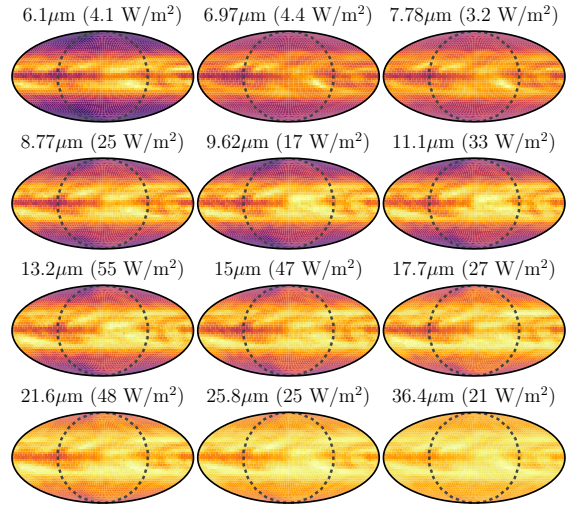
$e = 0.3$

$P_{\text{rot}} = 1 \text{ d}$

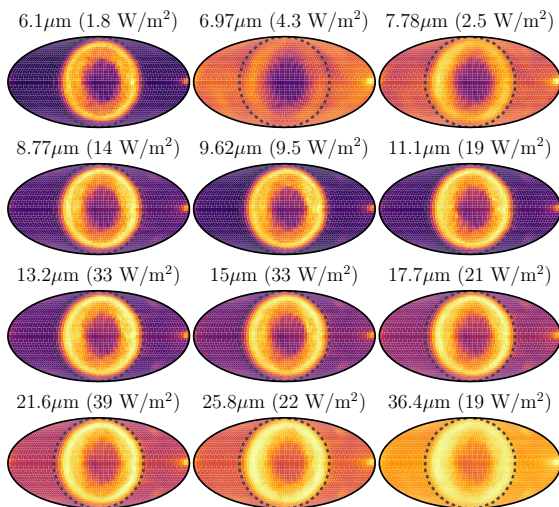


$e = 0.6$

$P_{\text{rot}} = 1 \text{ d}$



$P_{\text{rot}} = P_{\text{PSR}}$



$P_{\text{rot}} = P_{\text{PSR}}$

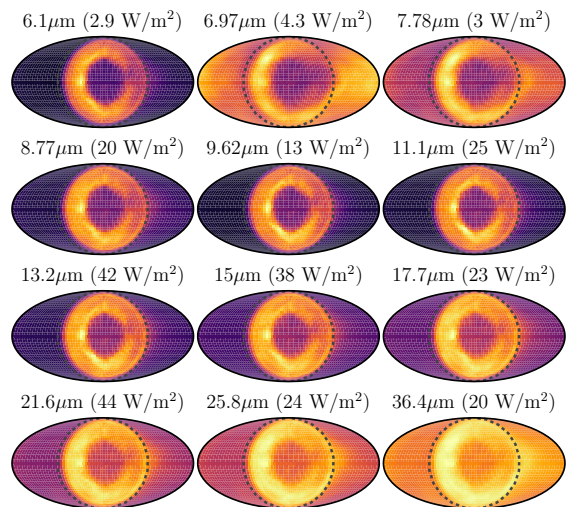
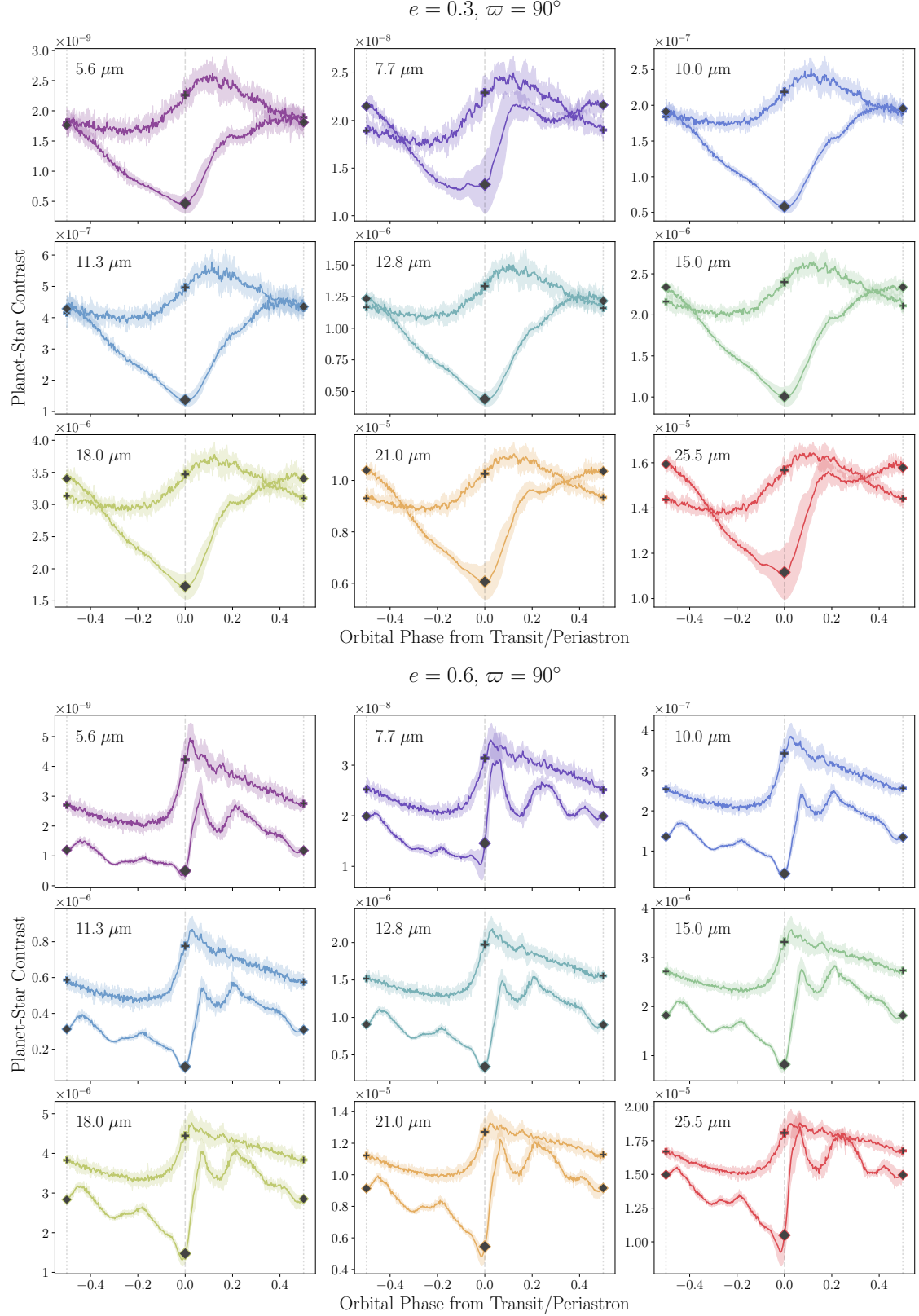


**Figure 7.** Global outgoing flux at the top of the atmosphere for a range of infrared bands from the ExoCAM model (Bands 7–18 in Table 2), for each of the two rotation periods and orbital eccentricities, during periastron. The dotted lines delineate the star-facing hemisphere, which is centered in each plot. Each subplot has a color range with zero flux as black, and the brightest color given by the flux above each globe in parentheses.

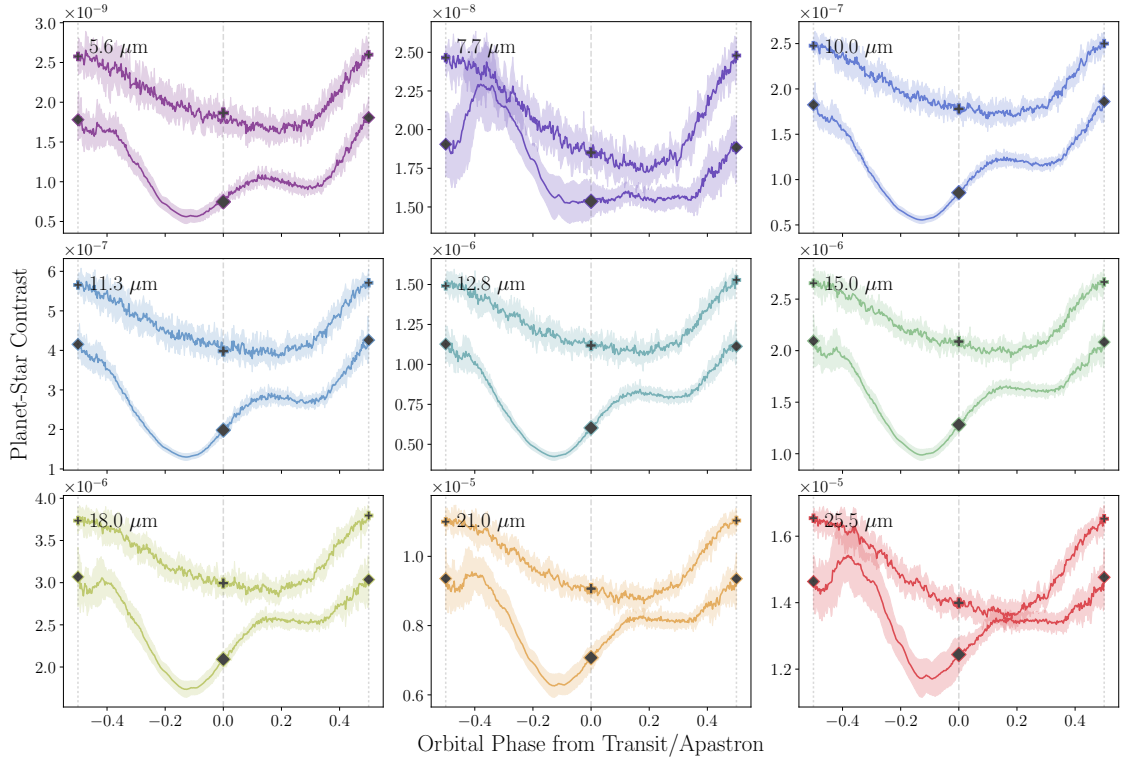
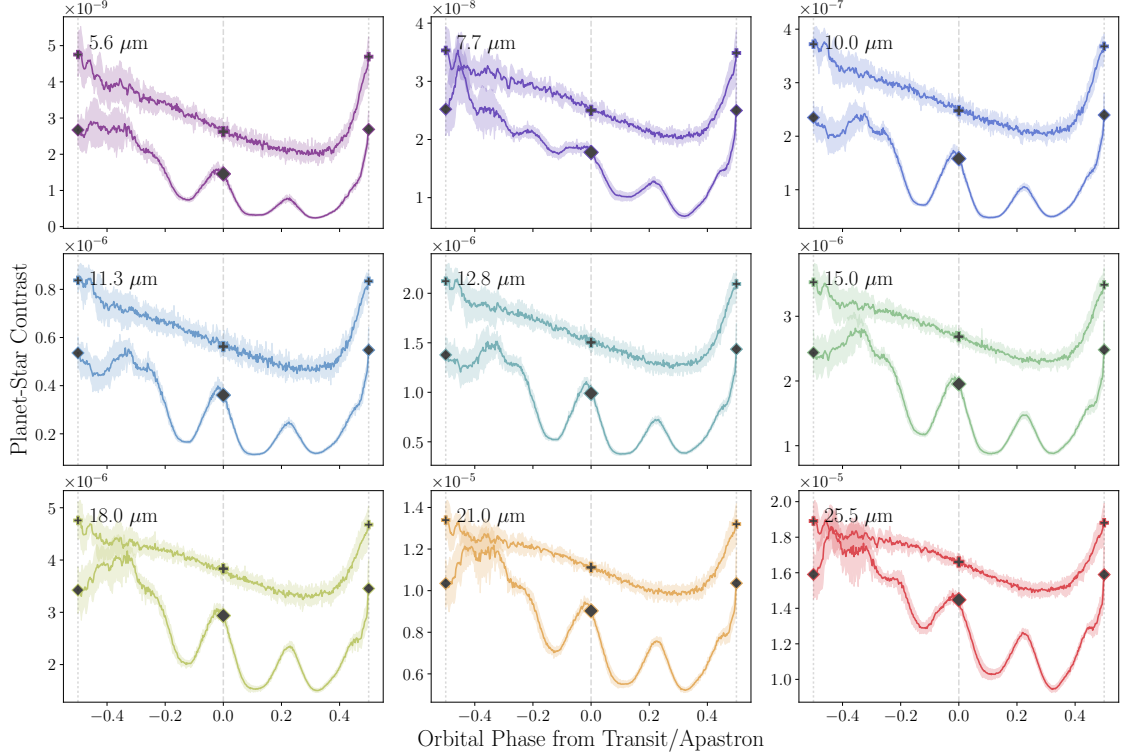
num mid-way between transit and eclipse. At  $e = 0.6$ , the pseudo-synchronous rotation period is short enough to allow a spike in each color near periastron for the slow rotator; large differences with the fast rotator thus occur about four times throughout the orbit consistent with the roughly 4:1 ratio of rotational to orbital periods. The  $e = 0.6$  color curves exhibit fairly some variations from orbit to orbit, but one persistent feature is

the set of secondary dips/peaks (depending on color), which correspond to the spin-orbit ratio.

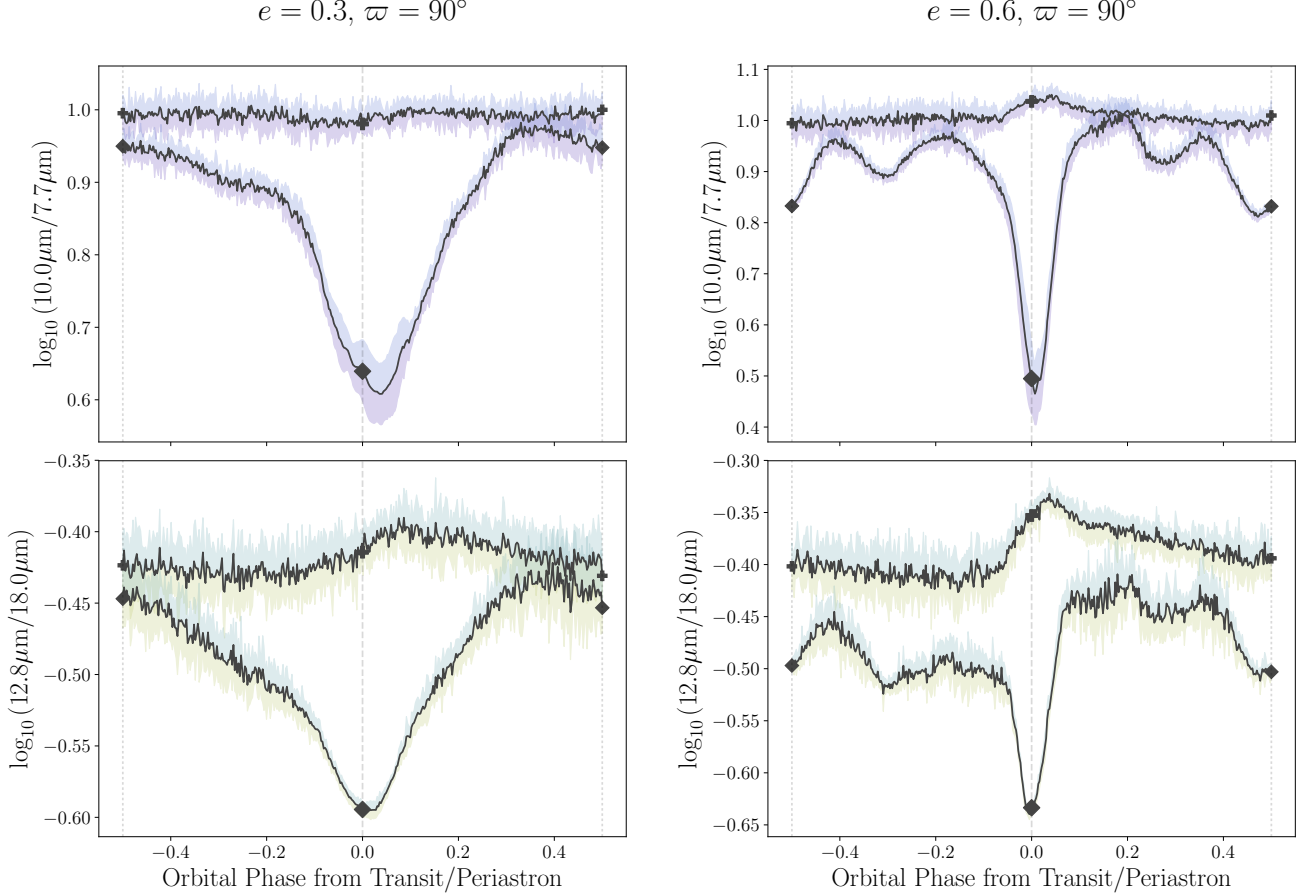
Despite limiting our analysis of full-orbit photometry to two extreme cases of  $\varpi = 90^\circ$  and  $270^\circ$ , it is relatively straightforward to predict the eclipse depths for the entire range of possible observing longitudes (Figure 12). The variations in eclipse depths in both cases with longitude only show minor variations relative to



**Figure 8.** Simulated light curves for a viewing geometry such that the orbit is seen edge-on, and the planet transits during periastron. Each 3x3 grid represents one of the two orbital eccentricities. The light curves are plotted for each of the 9 MIRI bands of the upcoming James Webb Space Telescope. Within each plot, the light curve with plus-sign markers shows Earth-like rotation, and the curve with diamond markers shows pseudo-synchronous rotation. The solid color lines are the averages over the final 10 orbits, and the surrounding shaded region represents the range of fluxes over the orbits.

$e = 0.3, \varpi = 270^\circ$ 

 $e = 0.6, \varpi = 270^\circ$ 


**Figure 9.** Simulated light curves for a viewing geometry such that the orbit is seen edge-on, and the planet undergoes secondary eclipse during periastron. Each 3x3 grid represents one of the two orbital eccentricities. The light curves are plotted for each of the 9 MIRI bands of the upcoming James Webb Space Telescope. Within each plot, the light curve with plus-sign markers shows Earth-like rotation, and the curve with diamond markers shows pseudo-synchronous rotation. The solid black lines are the averages over the final 10 orbits, and the surrounding shaded region represents the range of fluxes over the orbits.



**Figure 10.** Ratios of a selection of the planet-star contrasts shown in the light curves of Figure 8, where the planet transits during periastron. Within each plot, the light curve with plus-sign markers shows Earth-like rotation, and the curve with diamond markers shows pseudo-synchronous rotation. The solid black lines are the averages over the final 10 orbits, and the surrounding shaded region represents the range of fluxes over the orbits. The choice of colors for these regions is purely to illustrate the fluxes used for each ratio.

the ranges seen in Figures 10 and 11. Given this, it would be comparatively difficult to distinguish the scale of rotation from eclipse depths alone; therefore we also examine the night-side fluxes one would observe during transit (Figure 13). Here we gain the advantage of the strong day-night water-induced contrasts seen in the pseudo-synchronous cases. From these, we suggest that observations of day-side fluxes during/near eclipse, coupled with night-side fluxes during/near transit, could help discern these two cases.

The variations in eclipse depths with viewing geometry show a similar qualitative behavior as the phase curves with respect to rotation: the fast rotators exhibit a much weaker dependence on the observing angle than the pseudo-synchronous cases. This further suggests that, while maximizing the observing time would maximize the ability to discern between these cases, for a wide range of viewing geometries a pair of eclipse depths could hint at the broad timescale of rotation.

#### 4.2.4. Effects of Mixed Layer Ocean Depth

The previous analysis assumed a uniform ocean depth of 50 meters. We expect that, since the observable metrics we have constructed rely on absorption characteristics of water, the depth can readily affect both the quantity and temperature of precipitable water. To explore the broad effect of the depth on our results, we re-run the  $e = 0.3$  cases with ocean mixed layers depths of 10 meters. The ice cover and cloud density increase slightly relative to the 50-meter case at both extremes of the orbit, for both rotation periods. We plot the 10-meter light curve ratios, analogous to Figures 10 and 11, in Figures 14–15. While the simulated MIRI light curves do not change appreciably in the scale of planet-star contrasts, we find that, in line with the increased orbital sensitivity seen in the vertical profiles, the Earth-rotation curves do exhibit stronger amplitudes of phase variations compared with their deeper ocean counterparts. This vari-

$e = 0.3, \varpi = 270^\circ$

$e = 0.6, \varpi = 270^\circ$

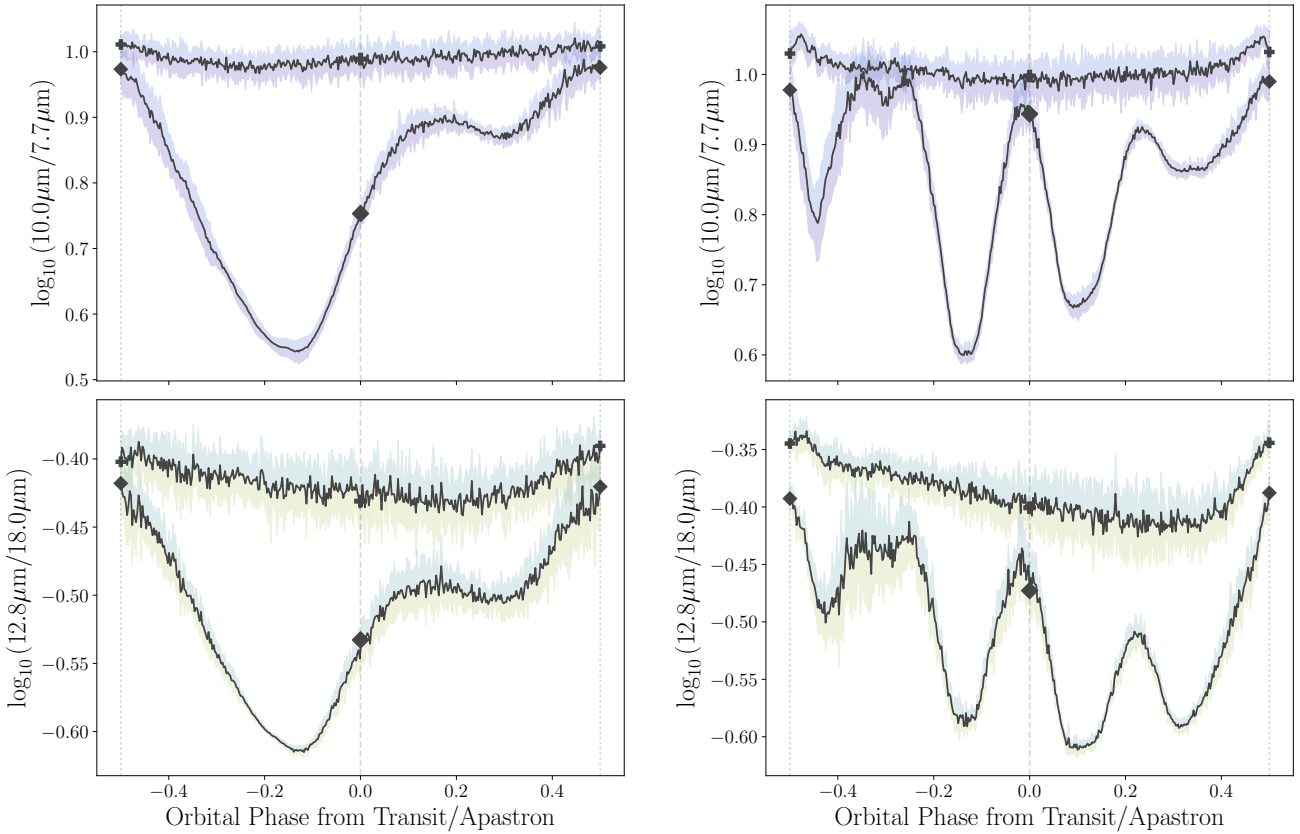


**Figure 11.** Ratios of a selection of the planet-star contrasts shown in the light curves of Figure 9, where the planet transits during apastron. Within each plot, the light curve with plus-sign markers shows Earth-like rotation, and the curve with diamond markers shows pseudo-synchronous rotation. The solid color lines are the averages over the final 10 orbits, and the surrounding shaded region represents the range of fluxes over the orbits. The choice of colors for these regions is purely to illustrate the fluxes used for each ratio.

ation is nevertheless still small compared with the average difference between rotation cases at fixed depth. The water-induced features in the pseudo-synchronous case are more pronounced here, which accentuates the post-transit responses in the flux ratios, especially for the redder ratio. From this we conclude that while the ocean depth has some effect on the observables, both the quality and quantity of differences are not significant enough to affect our results.

## 5. DISCUSSION

We show that, for a GCM modified to model a flat-topography ocean planet, differences in the scale of rotation rate between two physically-motivated values could be discernible from mid-infrared phase photometry of sufficient signal-to-noise to reach a contrast of at least 1 ppm relative to the host star. We explicitly model two contrasting viewing geometries and demonstrate that differences of order  $\sim 0.3\text{--}0.4$  dex in photometric con-

trast ratios would be distinguishable with a combination of broadband flux observations during transit and secondary eclipse. These differences are caused by the strong dependence of phase curve features, at particular wavelengths, on the concentration of upper-tropospheric water vapor. We have shown that, while any day-night contrasts in the temperature are restricted to layers near the planets' surfaces, day-night contrasts in atmospheric moisture concentration become very strong well into the upper atmosphere for rotation with periods comparable with the orbital period. These characteristic contrasts impart significant additional variations in those specific photometric bands which contain water absorption features, most notably in the MIRI band centered at  $7.7\text{ }\mu\text{m}$ , but also broadly in the mid-infrared beyond approximately  $20\text{ }\mu\text{m}$ .

While we have attempted to explore a constrained problem with as few added assumptions as possible, we acknowledge that we have not considered other dy-

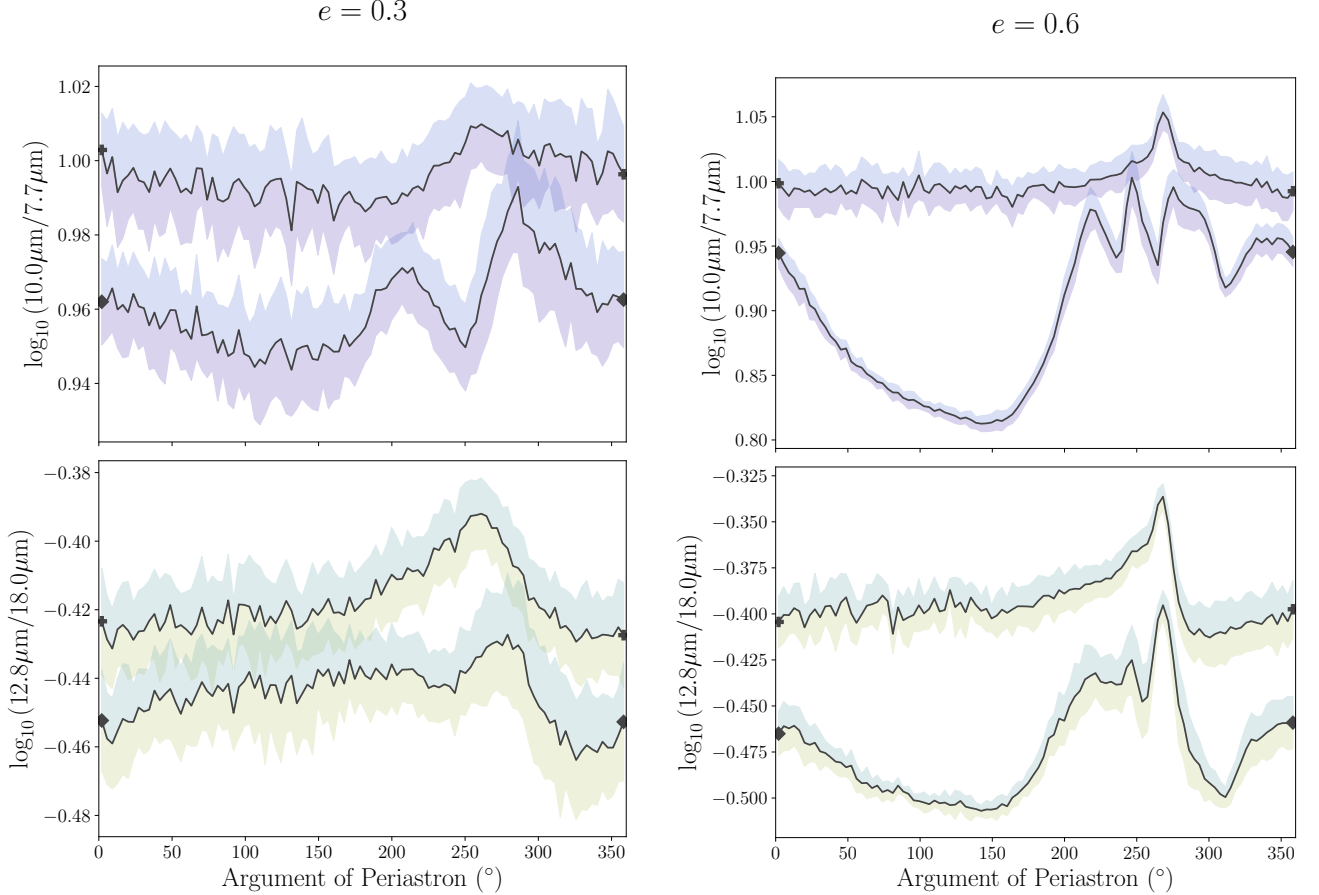


**Figure 12.** Predicted eclipse depth ratios for the range of possible longitudes of periastron relative to an observer. The quantities plotted are identical to those in Figures 10 and 11. The solid color lines are the averages over the final 10 orbits, and the surrounding shaded region represents the range of fluxes over the orbits. The choice of colors for these regions is purely to illustrate the fluxes used for each ratio.

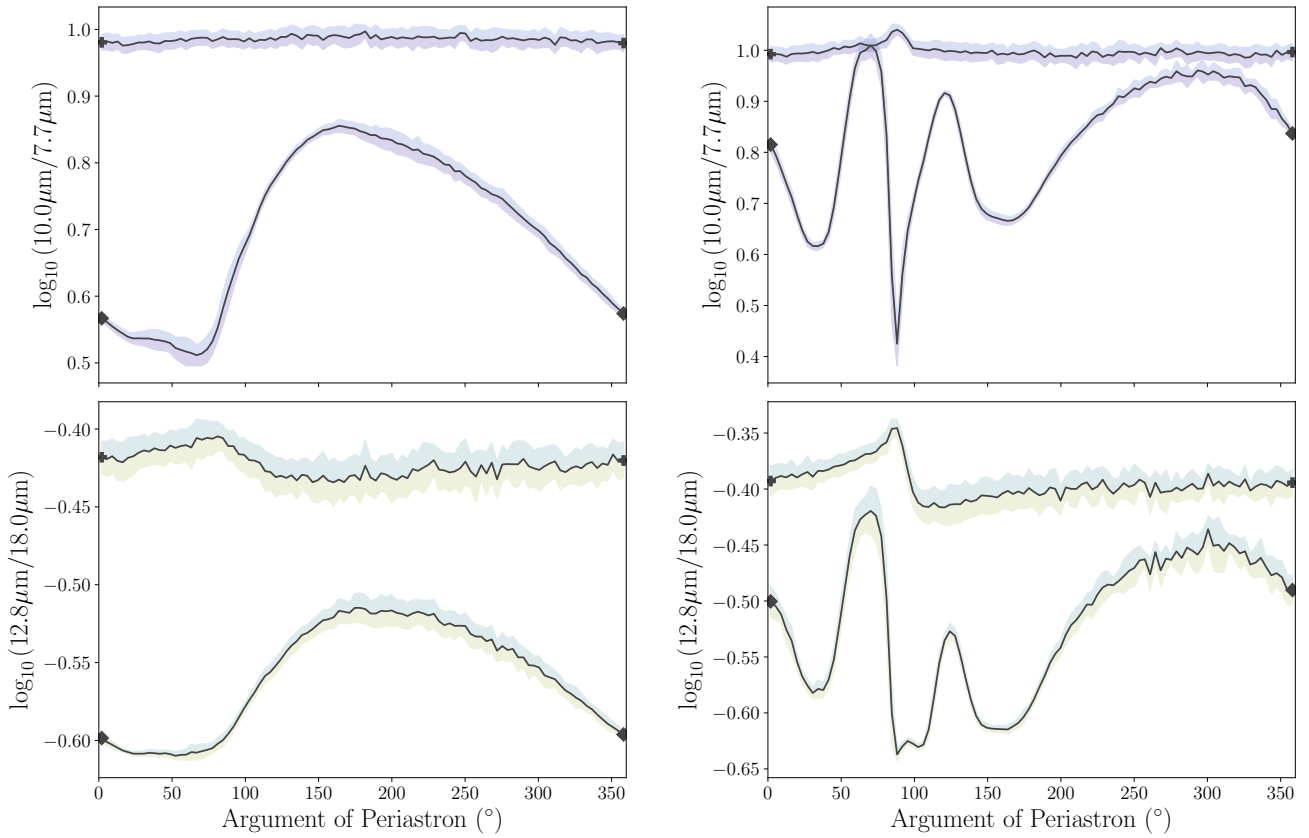
nodynamical and atmospheric effects that might otherwise contribute observables with an amplitude comparable with our phase variations. In particular, we do not take into account the effects of tidal heating/dissipation, which could induce an additional forcing term to our systems. Additionally, the construction of transit and eclipse depths implies a narrow range of observed orbital inclinations, and we have assumed perfectly edge-on orbits in the construction of our predicted observables. This is a reflection of the detection bias inherent to transiting exoplanets; however, phase variations should persist even for non-transiting planets. We have

also restricted ourselves to studying systems with solar-type host stars; studies such as Yang et al. (2013) predict that at instellations higher than Earth’s, the phase variations can effectively invert from the predictions at Earth-like instellation, so we emphasize our conclusions are limited to solar analogs. Finally, we have assumed zero planet obliquity; the interplay between the effects of the rotation and orbit in setting the periodicities in heating in particular would be greatly sensitive to the orientation of the spin axis. In a future work we will examine how these results vary for a variety of conditions for temperate terrestrial exoplanets.

## APPENDIX

### A. THEORETICAL ESTIMATES OF COLORS FOR PERFECT BLACKBODIES

We constructed colors by taking the ratio of the planet-star contrast in one wavelength band to the planet-star contrast in a second wavelength band; we chose one band in a spectral region that is highly sensitive to water vapor absorption and the other in the water vapor window. Here we illustrate the utility of these colors by examining the idealized case where the emission in each band comes from a perfect black body.

$e = 0.3$  $e = 0.6$ 

**Figure 13.** Predicted ratios of the observed night-side contrasts during transit for the range of possible longitudes of periastron relative to an observer. The quantities plotted are identical to those in Figures 10 and 11. The solid color lines are the averages over the final 10 orbits, and the surrounding shaded region represents the range of fluxes over the orbits. The choice of colors for these regions is purely to illustrate the fluxes used for each ratio.

We first note that for the planet-star contrast  $P(\lambda, T)$  at a given wavelength  $\lambda$  and planetary temperature  $T$ ,

$$P(\lambda, T) \propto \frac{B_\lambda(T)}{B_\lambda(T_\star)} \quad (\text{A1})$$

where  $T_\star$  is the emission temperature of the star, which we also approximate as a perfect black body. The quantity  $P(\lambda, T)$  is a thermal idealization of an individual light curve (e.g. Figure 8). A color is then the ratio of the planet-star contrast at wavelength  $\lambda_1$  to that at wavelength  $\lambda_2$ ,

$$C(\lambda_1, \lambda_2) = \frac{P(\lambda_1, T_1)}{P(\lambda_2, T_2)} = \frac{B_{\lambda_1}(T_1)B_{\lambda_2}(T_\star)}{B_{\lambda_2}(T_2)B_{\lambda_1}(T_\star)}. \quad (\text{A2})$$

We assume that the emission at wavelength  $\lambda_i$  comes entirely from a layer of the atmosphere with temperature  $T_i$ , and plot  $C$  as a function of  $T_1, T_2$  for two particular combinations of wavelengths (Figure 16). For  $(\lambda_1, \lambda_2) = (10.0 \mu\text{m}, 7.7 \mu\text{m})$ , lines of constant  $C$  are slightly less steep than the one-to-one line. For a uniform warming of  $T_1$  and  $T_2$ , an increase of 100 K is thus required to produce a decrease in  $C$  of about 0.2 to 0.3 dex, while the same change in  $C$  can be achieved by a differential warming in those temperatures of only 10–15 K. Similar behavior is exhibited for  $(\lambda_1, \lambda_2) = (12.8 \mu\text{m}, 18.0 \mu\text{m})$ , except because of the reverse ordering of wavelengths, a uniform warming of 100 K produces an increase of about 0.2 dex, while that same increase can be achieved by a differential warming of 10–15 K. Thus,  $C$  is relatively insensitive to a uniform planetary warming or cooling, and is about an order of magnitude more sensitive to differential changes in the emission level of the two wavelengths chosen for  $C$ . For example, if one wavelength for  $C$

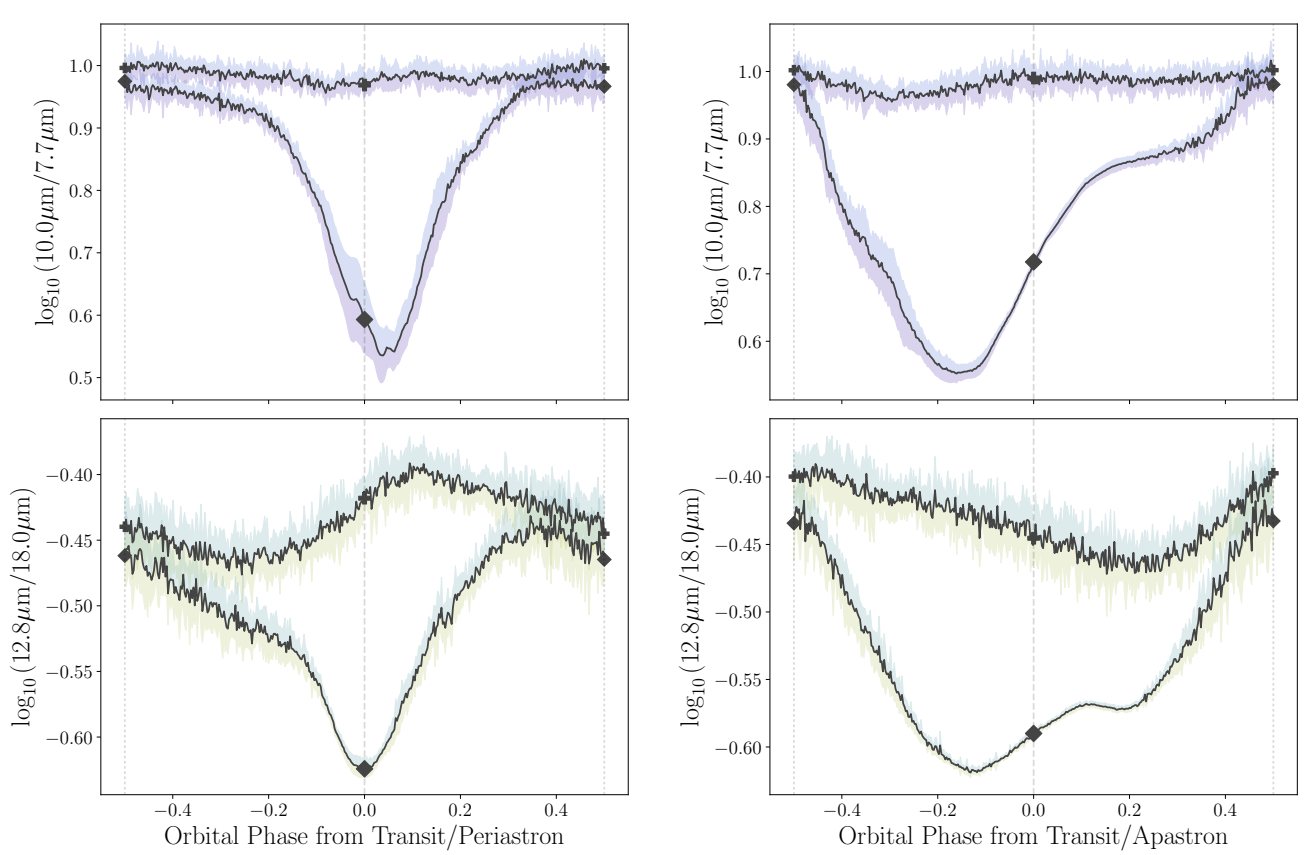


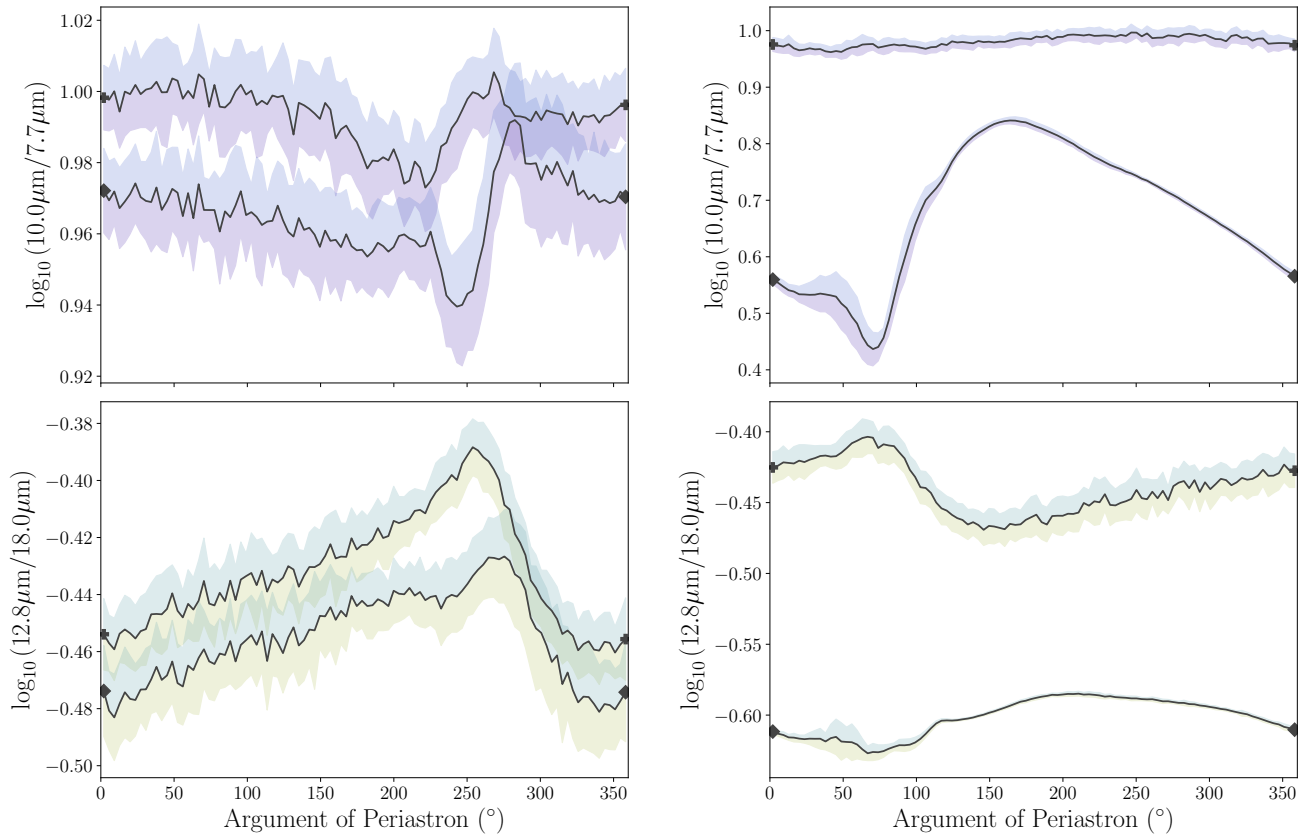
**Figure 14.** Same as Figures 10 (left) and 11 (right) for ocean depths of 10 meters, for  $e = 0.3$ .

is located in the water vapor window and the other in a spectral band with strong water vapor absorption, we would expect to see a large change in  $C$  as we move from viewing a dry side of the planet (where  $T_1$  and  $T_2$  are nearly the same) to viewing a humid side. The emission changes due to the water-specific features are able to dominate the color variations over the orbit-induced thermal color variations.

This material is based upon work supported by the National Aeronautics and Space Administration through the NASA Astrobiology Institute under Cooperative Agreement Notice NNH13ZDA017C issued through the Science Mission Directorate. We acknowledge support from the NASA Astrobiology Institute through a cooperative agreement between NASA Ames Research Center and Yale University.

We would like to thank Dr. Aomawa Shields, whose feedback with regard to model convergence criteria and dependence of results on ocean mixed layer depth helped the scientific rigor of this work.

*Software:* Astropy ([Astropy Collaboration et al. 2013](#)), Colorcet ([Kovesi 2015](#)), Jupyter ([Kluyver et al. 2016](#)), Matplotlib ([Hunter 2007](#)), Numpy ([van der Walt et al. 2011](#)), Paletton ([Staníček 2018](#)), Scipy ([Jones et al. 2001](#))

$e = 0.3$  $e = 0.3$ 

**Figure 15.** Same as Figures 12 (left) and 13 (right),  $e = 0.3$ , but for ocean depths of 10 meters.

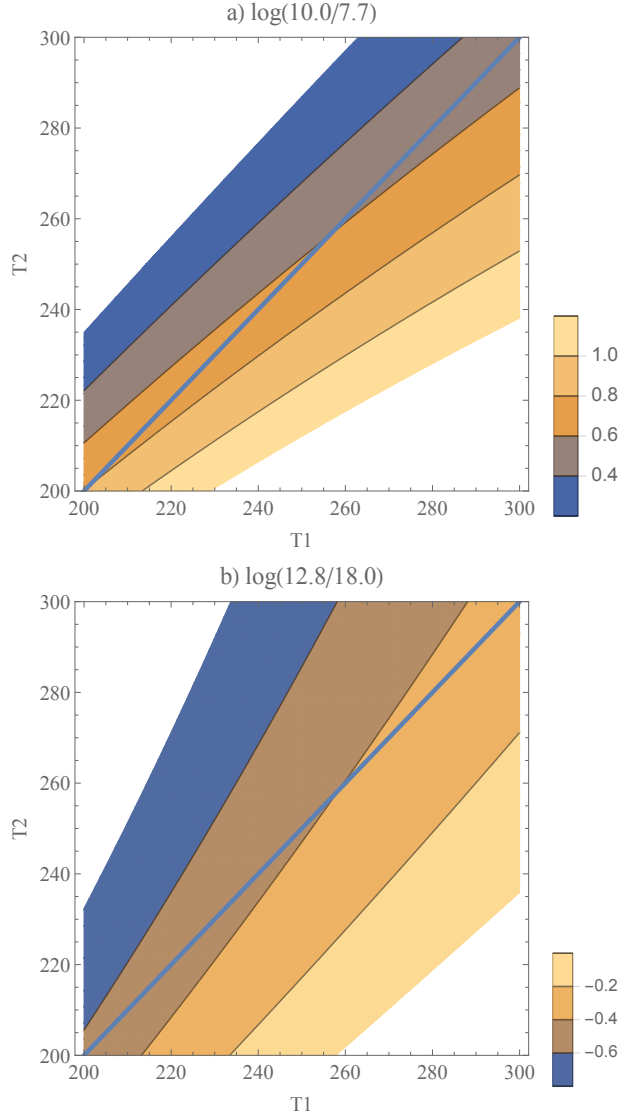


**Figure 16.** Theoretical “colors” for two perfect black bodies at temperatures  $T_1$  and  $T_2$ , in K. As described in the text, these colors are constructed using the Planck function and assuming a black body star at 6000 K, and use wavelengths of a) 10.0 and 7.7  $\mu\text{m}$ , and b) 12.8 and 18.0  $\mu\text{m}$ . The gradient represents the values of the color given in the title, and the blue line shows where  $T_1 = T_2$ .

## REFERENCES

- Adams, A. D., & Kane, S. R. 2016, *Astron. J.*, 152, 4, doi: [10.3847/0004-6256/152/1/4](https://doi.org/10.3847/0004-6256/152/1/4)
- Astropy Collaboration, Robitaille, T., Tollerud, E., et al. 2013, *A&A*, 558, A33, doi: [10.1051/0004-6361/201322068](https://doi.org/10.1051/0004-6361/201322068)
- Barnes, J., Haberle, R., Pollack, J., Lee, H., & Schaeffer, J. 1996, *J. Geophys. Res.*, 101, 12753, doi: [10.1029/96JE00179](https://doi.org/10.1029/96JE00179)
- Barnes, J., Pollack, J., Haberle, R., et al. 1993, *J. Geophys. Res.*, 98, 3125, doi: [10.1029/92JE02935](https://doi.org/10.1029/92JE02935)
- Barnes, J. R., & Haberle, R. M. 1996, *J. Atmos. Sci.*, 53, 3143, doi: [10.1175/1520-0469\(1996\)053<3143:TMZMCA>2.0.CO;2](https://doi.org/10.1175/1520-0469(1996)053<3143:TMZMCA>2.0.CO;2)
- Barnes, R., Raymond, S., Jackson, B., & Greenberg, R. 2008, *Astrobiology*, 8, 557, doi: [10.1089/ast.2007.0204](https://doi.org/10.1089/ast.2007.0204)
- Bitz, C. M., Shell, K. M., Gent, P. R., et al. 2012, *J. Clim.*, 25, 3053, doi: [10.1175/JCLI-D-11-00290.1](https://doi.org/10.1175/JCLI-D-11-00290.1)
- Bolmont, E., Libert, A.-S., Leconte, J., & Selsis, F. 2016a, *A&A*, 591, A106, doi: [10.1051/0004-6361/201628073](https://doi.org/10.1051/0004-6361/201628073)
- . 2016b, 1, doi: [10.1051/0004-6361/201628073](https://doi.org/10.1051/0004-6361/201628073)
- Cullum, J., Stevens, D., & Joshi, M. 2014, *Astrobiology*, 14, 645, doi: [10.1089/ast.2014.1171](https://doi.org/10.1089/ast.2014.1171)
- de Wit, J., Lewis, N., Langton, J., et al. 2016, *ApJL*, 820, L33, doi: [10.3847/2041-8205/820/2/L33](https://doi.org/10.3847/2041-8205/820/2/L33)
- Deitrick, R., Barnes, R., Bitz, C., et al. 2018, *Astron. J.*, 155, 266, doi: [10.3847/1538-3881/aac214](https://doi.org/10.3847/1538-3881/aac214)
- Dressing, C., Spiegel, D., Scharf, C., Menou, K., & Raymond, S. 2010, *ApJ*, 721, 1295, doi: [10.1088/0004-637X/721/2/1295](https://doi.org/10.1088/0004-637X/721/2/1295)
- Forget, F., Wordsworth, R., Millour, E., et al. 2013, *Icarus*, 222, 81, doi: [10.1016/j.icarus.2012.10.019](https://doi.org/10.1016/j.icarus.2012.10.019)
- Forget, F., Hourdin, F., Fournier, R., et al. 1999, *J. Geophys. Res.*, 104, 24155, doi: [10.1029/1999JE001025](https://doi.org/10.1029/1999JE001025)
- Georgakarakos, N., Dobbs-Dixon, I., & Way, M. J. 2016, *Mon. Not. R. Astron. Soc.*, 461, 1512, doi: [10.1093/mnras/stw1378](https://doi.org/10.1093/mnras/stw1378)
- Glasse, A., Rieke, G., Bauwens, E., et al. 2015, *PASP*, 127, 686, doi: [10.1086/682259](https://doi.org/10.1086/682259)
- Goldreich, P., & Soter, S. 1966, *Icarus*, 5, 375, doi: [http://dx.doi.org/10.1016/0019-1035\(66\)90051-0](http://dx.doi.org/10.1016/0019-1035(66)90051-0)
- Haberle, R., Pollack, J., Barnes, J., et al. 1993, *J. Geophys. Res.*, 98, 3093, doi: [10.1029/92JE02946](https://doi.org/10.1029/92JE02946)
- Hunke E.C., L. W. H. 2008, CICE: The Los Alamos Sea Ice Model, Documentation and Software User's Manual, Version 4.0, Tech. Rep. LA-CC-06-012, Los Alamos National Laboratory, Los Alamos, New Mexico
- Hunter, J. D. 2007, *Comput. Sci. Eng.*, 9, 90, doi: [10.1109/MCSE.2007.55](https://doi.org/10.1109/MCSE.2007.55)
- Hut, P. 1981, *A&A*, 99, 126
- Institute, S. T. S. 2017, JWST MIRI Filters and Dispersers. <https://jwst-docs.stsci.edu/display/JTI/MIRI+Filters+and+Dispersers>
- Jones, E., Oliphant, T., Peterson, P., & Others. 2001, SciPy: Open source scientific tools for Python. <http://www.scipy.org/>
- Joshi, M., Haberle, R., & Reynolds, R. 1997, *Icarus*, 129, 450, doi: [10.1006/icar.1997.5793](https://doi.org/10.1006/icar.1997.5793)
- Kane, S., & Gelino, D. 2012, *Astrobiology*, 12, 940, doi: [10.1089/ast.2011.0798](https://doi.org/10.1089/ast.2011.0798)
- Kasting, J., Whitmire, D., & Reynolds, R. 1993, *Icarus*, 101, 108, doi: [10.1006/icar.1993.1010](https://doi.org/10.1006/icar.1993.1010)
- Kluyver, T., Ragan-Kelley, B., Perez, F., et al. 2016, IOS Press, 87
- Kopparapu, R., Ramirez, R., SchottelKotte, J., et al. 2014, *ApJL*, 787, L29, doi: [10.1088/2041-8205/787/2/L29](https://doi.org/10.1088/2041-8205/787/2/L29)
- Kopparapu, R., Wolf, E. T., Arney, G., et al. 2017, *Astrophys. J.*, 845, 5, doi: [10.3847/1538-4357/aa7cf9](https://doi.org/10.3847/1538-4357/aa7cf9)
- Kopparapu, R., Ramirez, R., Kasting, J., et al. 2013, *ApJ*, 765, 131, doi: [10.1088/0004-637X/765/2/131](https://doi.org/10.1088/0004-637X/765/2/131)
- Kovesi, P. 2015, ArXiv e-prints. <https://arxiv.org/abs/1509.03700>
- Kozai, Y. 1962, *AJ*, 67, 591, doi: [10.1086/108790](https://doi.org/10.1086/108790)
- Lebonnois, S., Hourdin, F., Eymet, V., et al. 2010, *J. Geophys. Res.*, 115, E06006, doi: [10.1029/2009JE003458](https://doi.org/10.1029/2009JE003458)
- Lewis, N., Parmentier, V., Kataria, T., et al. 2017, ArXiv e-prints. <https://arxiv.org/abs/1706.00466>
- Lidov, M. 1962, *Planet. Space Sci.*, 9, 719, doi: [10.1016/0032-0633\(62\)90129-0](https://doi.org/10.1016/0032-0633(62)90129-0)
- Lin, S., & Rood, R. 1997, *Q. J. R. Meteorol. Soc.*, 123, 2477, doi: [10.1002/qj.49712354416](https://doi.org/10.1002/qj.49712354416)
- Lin, S.-J., & Rood, R. 1996, *Mon. Weather Rev.*, 124, 2046, doi: [10.1175/1520-0493\(1996\)124<2046:MFFSLT>2.0.CO;2](https://doi.org/10.1175/1520-0493(1996)124<2046:MFFSLT>2.0.CO;2)
- Linsenmeier, M., Pascale, S., & Lucarini, V. 2015, *Planet. Space Sci.*, 105, 43, doi: [10.1016/j.pss.2014.11.003](https://doi.org/10.1016/j.pss.2014.11.003)
- Makarov, V. V., & Efroimsky, M. 2013, *Astrophys. J.*, 764, 27, doi: [10.1088/0004-637X/764/1/27](https://doi.org/10.1088/0004-637X/764/1/27)
- Merlis, T., & Schneider, T. 2010, *J. Adv. Model. Earth Syst.*, 2, 13, doi: [10.3894/JAMES.2010.2.13](https://doi.org/10.3894/JAMES.2010.2.13)
- Murray, C., & Dermott, S. 1999, Solar system dynamics
- Neale, R. B., Chen, C.-C., Gettelman, A., et al. 2010, Description of the NCAR community atmosphere model (CAM 5.0), Tech. rep.
- O'Gorman, P., & Schneider, T. 2008, *J. Clim.*, 21, 3815, doi: [10.1175/2007JCLI2065.1](https://doi.org/10.1175/2007JCLI2065.1)
- Rieke, G., Wright, G., Böker, T., et al. 2015, *PASP*, 127, 584, doi: [10.1086/682258](https://doi.org/10.1086/682258)

- Rossow, W. 1983, *J. Atmos. Sci.*, 40, 273,  
doi: [10.1175/1520-0469\(1983\)040\(0273:AGCMOA\)2.0.CO;2](https://doi.org/10.1175/1520-0469(1983)040(0273:AGCMOA)2.0.CO;2)
- Shields, A., Bitz, C., Meadows, V., Joshi, M., & Robinson, T. 2014, *ApJL*, 785, L9,  
doi: [10.1088/2041-8205/785/1/L9](https://doi.org/10.1088/2041-8205/785/1/L9)
- Shields, A., Meadows, V., Bitz, C., et al. 2013, *Astrobiology*, 13, 715, doi: [10.1089/ast.2012.0961](https://doi.org/10.1089/ast.2012.0961)
- Shields, A. L. A., Barnes, R., Agol, E., et al. 2016, *Astrobiology*, 16, 443, doi: [10.1089/ast.2015.1353](https://doi.org/10.1089/ast.2015.1353)
- Showman, A., & Guillot, T. 2002, *A&A*, 385, 166,  
doi: [10.1051/0004-6361:20020101](https://doi.org/10.1051/0004-6361:20020101)
- Spiegel, D., Raymond, S., Dressing, C., Scharf, C., & Mitchell, J. 2010, *ApJ*, 721, 1308,  
doi: [10.1088/0004-637X/721/2/1308](https://doi.org/10.1088/0004-637X/721/2/1308)
- Staníček, P. 2018, Paletton, the color scheme designer.  
<http://paletton.com/>
- van der Walt, S., Colbert, S. C., & Varoquaux, G. 2011, *Comput. Sci. Eng.*, 13, 22, doi: [10.1109/MCSE.2011.37](https://doi.org/10.1109/MCSE.2011.37)
- Wang, Y., Liu, Y., Tian, F., et al. 2016, *ApJL*, 823, L20,  
doi: [10.3847/2041-8205/823/1/L20](https://doi.org/10.3847/2041-8205/823/1/L20)
- Way, M. J., & Georgakarakos, N. 2016, *Astrophys. J. Lett.*, 835, 1, doi: [10.3847/2041-8213/835/1/L1](https://doi.org/10.3847/2041-8213/835/1/L1)
- Werner, M., Roellig, T., Low, F., et al. 2004, *ApJS*, 154, 1,  
doi: [10.1086/422992](https://doi.org/10.1086/422992)
- Williams, D. M., & Pollard, D. 2002, *Int. J. Astrobiol.*, 1, 61, doi: [10.1017/S1473550402001064](https://doi.org/10.1017/S1473550402001064)
- Wolf, E., & Toon, O. 2013, *Astrobiology*, 13, 656,  
doi: [10.1089/ast.2012.0936](https://doi.org/10.1089/ast.2012.0936)
- . 2014, *Geophys. Res. Lett.*, 41, 167,  
doi: [10.1002/2013GL058376](https://doi.org/10.1002/2013GL058376)
- . 2015, *J. Geophys. Res.*, 120, 5775,  
doi: [10.1002/2015JD023302](https://doi.org/10.1002/2015JD023302)
- Wright, G., Wright, D., Goodson, G., et al. 2015, *PASP*, 127, 595, doi: [10.1086/682253](https://doi.org/10.1086/682253)
- Yang, J., Cowan, N., & Abbot, D. 2013, *ApJL*, 771, L45,  
doi: [10.1088/2041-8205/771/2/L45](https://doi.org/10.1088/2041-8205/771/2/L45)
- Zalucha, A., Plumb, R., & Wilson, R. 2010, *J. Atmos. Sci.*, 67, 673, doi: [10.1175/2009JAS3130.1](https://doi.org/10.1175/2009JAS3130.1)